ERNEST ORLANDO LAWRENCE BERKELEY NATIONAL LABORATORY	Cat Code: **MU1010**	**ENGINEERING NOTE**	Serial: **10507**	Rev: **A**	Page: 1 of 72
Author(s): **F. Trillaud, S. Virostek, M.A. Green, M.S. Zisman**	Department: **Mechanical Engineering**		Location: **Berkeley**	Date: 06/28/2010	
Title: **MICE spectrometer** **Thermal analysis and parametric studies**					

ERNEST ORLANDO LAWRENCE
BERKELEY NATIONAL LABORATORY

LBL TECHNICAL NOTE

MICE spectrometer:

Thermal simulations and parametric studies

Author:
Frederic TRILLAUD*

Co-authors:
Michael A. GREEN*
Steve P. VIROSTEK*
Michael S. ZISMAN**

Senior engineer:
Steve P. VIROSTEK

LBL project manager:
Michael S. ZISMAN

Monday 28th June, 2010

*: Engineering division.
**: Accelerator and Fusion Research Division.

The authors would like to thank Dr. Soren Prestemon and Dr. Diego Arbalaez for the fruitful discussions on the details of the numerical model.

Contents

List of Figures

List of Tables

Nomenclature

ϵ_{pf}	Criterion for fixed point iterations
$\mathbf{Q}$	Vector of normalized thermal heat loads: radiation, conduction and Joule heating [W/m^3]
$\mathbf{T}$	Vector composed of temperatures interpolated on the mesh
$\mathcal{A}$	Magnetic potential vector [V.s/m]
C	Specific heat capacity [J/K-kg]
C_{eq}	Specific heat capacity normalized to the actual geometry [J/K-kg]
$\mathcal{J}$	Vector of current density [A/m^2]
$\mathcal{K}$	Thermal conductivity [W/m-K]
$\mathcal{K}_1$	Thermal conductivity of OFHC copper $[W/m-K]$
$\mathcal{K}_2$	Thermal conductivity of 11%AuAg $[W/m-K]$
$\mathcal{K}_{\text{av}}$	Average thermal conductivity [W/m-K]
$\mathcal{K}_{\text{eq}}$	Thermal conductivity normalized to the actual geometry [W/m-K]
$\mathcal{K}_{\text{ins}}$	Equivalent thermal conductivity of super-insulation [W/m-K]
$\mathcal{L}$	Inductance [H]
$\mathcal{V}$	Volume $[m^3$
ω_{i}, F_{i}, β, e_{i}, g_{i}	Variables to simplify algebric calculations, $\forall i \in \{1, 2, 3\}$
Φ	Thermal heat flux [W]
ρ_1	Electrical resistivity of OFHC copper [Ω-m
ρ_2	Electrical resistivity of 11%AuAg [Ω-m
τ	Magnetic time constant [s]

$\tilde{\mathcal{K}}(T, B, RRR)$ Tensor of thermal conductivity [W/m.K]

A Cross-sectional area [m^2]

a, b, c and d Constants of integration

A_r Area of cold wall for heat radiation computation [m^2]

d Optimum density of super-insulation layers

e Total thickness of super-insulation layers

h Equivalent mean heat transfer coefficient derived from the mean thermal conductivity [2] given for super-insulation [W/K-m^2]

I Transport current [A]

L Length[m]

n Total number of layers of super-insulation

Q_1 Heat load at the first stage of two-stage cryo-refrigerators [W]

Q_2 Heat load at the second stage of two-stage cryo-refrigerators [W]

Q_{hi} Known values of the heat load extracted form the map of the two-stage cryo-refrigerator: upper value [W]

Q_i Computed values of the heat loads at the stages of the two-stage cryo-refrigerators

Q_{li} Known values of the heat load extracted form the map of the two-stage cryo-refrigerator: lower values [W]

Q_r Heat load by radiation [W]

R Electrical resistance of circuitry [Ω]

R Thermal resistance [K/W]

t Time [s]

$T(\phi(T_n))$ Estimation of temperature at time step under a fixed point scheme [K]

T_{bc} Boundary condition: fixed temperatures [K]

T_c Temperature of cold wall for heat radiation computation [K]

T_{ij} Temperature corresponding to the known values of heat load closest to the computed heat load value, $\forall(i, j) \in 1, 2, 3, 4$ [K]

T_n Temperature at step n [K]

T_{w}	Temperature of warm wall for heat radiation computation [K]
T_1	Interpolated value of temperature for first stage heat load [K]
T_{h1}	Temperature corresponding to the average heat load on the lower side [K]
T_{l1}	Temperature corresponding to the average heat load on the upper side [K]
V	Voltage at the terminals of the power supplies [V]
x_1	Fraction of first stage heat load
x_2	Fraction of second stage heat load
x_{cp}	Geometrical fraction to adjust volumes to actual geometries
x_{tc}	Geometrical fraction to adjust dimensions to actual geometry
z_1	Length of OFHC copper lead [m]
z_2	Length of 11%AuAg [m]

Chapter 1

Introduction

This report deals with a parametric study of the cryo-refrigeration system of the spectrometers to be used by the international Muon Ionization Cooling Experiment (MICE) [3]. In collaboration with the Ernesto Lawrence Berkeley National Laboratory (LBL), a private company, WangNMR, Inc. [4], has been designing and building two spectrometers. They are constituted of 5 solenoids made of NbTi. It includes cryogenic components, and a magnet protection and detection system.
During the "training" of the first spectrometer, some issues arose during energization leading to the burn out of one of the High Temperature Superconducting (HTS) leads. The temperature sensors located across the device showed values larger than expected. To understand such a complex system, it appeared then helpful to refine the thermal analysis which has been undergone during the design phase. Consequently, beginning in mid 2009, parallel efforts have been conducted to address potential issues. Although most of the geometrical model has been initially based on the preliminary report produced by WangNMR Inc. [4], it incorporates some of the newest features at the time of this technical note.

The numerical model to perform the analysis has been written with CasT3M [1] which is dedicated to Finite Element computations [5]. The results have been analysed with Paraview Kitware [6]. Additional tools such as GNUplot [7], Qtiplot [8], Octave [9] and programming languages such as ANSI-C and C++ [10], have been used as well [2].

[1] A layout of the code and the user defined functions are given in appendix E (page 62).
[2] Some of the code listings are given in appendix F (page 65).

Chapter 2

Model of MICE spectrometer

The following chapter presents the assumptions and geometrical limitations used to implement the 3D numerical model. This model solves a heat balance equation with imposed temperatures and imposed heat fluxes at relevant boundaries. To backup parts of the model, analytical expression in the simplest cases have been derived as well (see appendices).
The system under study is composed of the thermal shield and its connections to the helium vessel and warm enclosure at 300 K.

2.1 Assumptions

The following assumptions have been considered:

- ◊ steady state,
- ◊ boundary conditions: fixed temperatures and heat fuxes,
- ◊ material properties dependent on temperature and magnetic flux density,
- ◊ idealized geometry,
- ◊ decoupling between magnetic and thermal problems.

Decoupling between magnetic and thermal problems: In this study, the influence of the dimensional variations due to temperature change and pure mechanical deformation is neglected.
Even if the material properties depend on temperature and magnetic field distributions, solely the temperature dependence is taken into account [1]. Indeed, the magnetic flux density is a relevant parameter for temperatures below 15 K or/and for the modelization of the High Temperature Superconducting leads.

Ideal geometry: The idealized geometry refers to the simplications chosen to create the geometrical model. Thus, the simulation represents an ideal case whose

[1] Despiste being implemented in the code, the dependence of the magnetic flux density has not been taken into account.

outputs correspond to the best responses of the system to thermal loads. Figure 2.1 18 shows side-by-side a picture of the actual spectrometer and its geometrical model. The limitations of this approach are further discussed in appendix B (page 47).

Material properties: The material properties are dependent on temperature, magnetic flux density, orientation and composition. In the following study, the dominant and available parameter is temperature. Figure 2.2 (page 19) shows a comparision between data from literature and the fits used by the authors. An agreement of less than 15% was achieved over the entire temperature range for all the materials considered hereby. The largest discrepancy is given by AL1100F at temperatures below 100 K.
Some of the geometries, even though appearing as lumped bodies, have been divided into sub-geometries corresponding to their respective materials to allow transient analysis (see appendix B, page 47).
Appendix A (page 42) summarizes the different parts of the spectrometer.

Boundary conditions: Fixed temperatures are ensured by lagrangian multipliers. These extra degrees of freedom represent the necessary thermal fluxes to respect the imposed values of boundary conditions.
This approach naturally enforces the first law of thermodynamics. The accuracy is mainly given by the mesh size as finer meshes lead to better agreements between the total heat load and the cooling. Table 2.1 (page 16) summirazes the numerical parameters pertaining to the simulation. Appendix G (page 69) gives a typical example of convergence.

Steady state: An existing solver based on a transient theta-method has been modified. The heat balance equation includes a time dependent term which vanishes by imposing the heat capacities equal to zero to enforce a steady state. This approach was validated on simple cases. It was found that a minimum of 15 time steps are necessary to converge to a steady thermal profile.

2.2 Heat balance equation

The program based on the ideal geometry solves sequentially the magnetic and heat balance equations. The equations to be integrated are the followings:

$$\begin{cases} \Delta \mathbf{A} + \mu_0 \mathbf{J} = 0, \\ div\left[\tilde{\mathcal{K}} \mathbf{grad}\,(\mathbf{T})\right] + \mathbf{Q} = 0. \end{cases} \tag{2.1}$$

with,

- ◊ $\tilde{\mathcal{K}}(T, B, RRR)$: tensor of thermal conductivity,
- ◊ **Q**: heat loads by radiation, conduction and Joule dissipation,
- ◊ **A**: magnetic potential vector,
- ◊ **J**: vector of current density.

The magnetic vector potential is integrated using Biot-Savart over the entire geometry. The obtained distribution of magnetic flux density is used to determine the appropriate material properties [2].
The heat load by radiation is taken into account through an equivalent mean heat transfer coefficient, h. This coefficient includes the presence of layers of super-insulations between the 300 K outer shell and the thermal shield. Based on Eckin's book [2], a typical layer density, d, has been chosen equal to 30 layers per centimeter for a total number of layers, n, equal to 50. Figure 2.3 (page 20) extracted from reference [2] shows the evolution of the mean apparent thermal conductivity of Aluminum foil plus fiberglass paper in residual nitrogen atmosphere. At pressures lower than 10^{-2} Pa, the equivalent thermal conductivity, $\mathcal{K}_{\text{ins}}$, reaches a plateau whose value is equal to 5×10^{-5} W/m.K. The corresponding linearized heat transfer coefficient is obtained as follows:

$$h \simeq \frac{\mathcal{K}_{\text{ins}}}{e}. \tag{2.2}$$

with,

$$e = \frac{n}{d}. \tag{2.3}$$

The heat load by radiation through the super-insulation is then expressed as:

$$Q_{\text{r}} \simeq hA_{\text{r}} \left(T_{\text{w}} - T_{\text{c}}\right). \tag{2.4}$$

The temperatures T_{w} and T_{c} correspond to the warm and the cold surfaces respectively. The surface to be considered is the cold surface, A_{r}.

2.3 Boundaries

Figure 2.4 (page 21) indicates the location of the different boundary conditions.

Current leads: In addition to fixed temperatures, heat fluxes equal to 4 W per leads maintain a temperature of about 300 K at their warm ends under the abscence of transport current.

[2] As mentioned previously, whereas it is implemented, it was not used in the study of the thermal shield.

Two-stage cryo-refrigerators: To simulate the cold extraction, a linear interpolation has been used to describe the mapping of the two-stage cryo-refrigerators. Assuming that the heat loads Q_1 and Q_2 are extracted by a cryo-refrigerator at its first and second stage, respectively, the following set of fractions are defined:

$$\begin{cases} x_1 = \dfrac{Q_1 - Q_{\mathrm{l}1}}{Q_{\mathrm{h}1} - Q_{\mathrm{l}1}}, \\ x_2 = \dfrac{Q_2 - Q_{\mathrm{l}2}}{Q_{\mathrm{h}2} - Q_{\mathrm{l}2}}. \end{cases} \tag{2.5}$$

where Q_{hi} and Q_{li} correspond to the known values of the map such that:

$$Q_{\mathrm{hi}} \geq Q_{\mathrm{i}} \geq Q_{\mathrm{li}}, \quad \forall i \in \{1, 2\}\,. \tag{2.6}$$

The temperature of the first stage of the cryo-refrigerator is then interpolated as follows:

$$T_1 \simeq T_{\mathrm{l}1} + x_2 \left(T_{\mathrm{h}1} - T_{\mathrm{l}1}\right). \tag{2.7}$$

with,

$$\begin{cases} T_{l1} \simeq T_{11} + x_1 \left(T_{12} - T_{\mathrm{l}1}\right), \\ T_{h1} \simeq T_{13} + x_1 \left(T_{14} - T_{13}\right). \end{cases} \tag{2.8}$$

An identical scheme has been implemented to interpolate the temperature at the second stage of the cryo-refrigerators. In the present case, a fixed value equal to 5 K has been chosen to focus on the behavior of the thermal shield and its related components. This approach is given possible because of the weak coupling between the stages.
To perform such interpolation and to ensure convergence, the data have been slightly modified to avoid the invariance of the temperature as a function of loads over certain portions of the map. A mild slope of less than 5% has been added. Table 2.2 (page 17) summarizes the values used in the simulation.

Table 2.1: Numerical parameters.

Parameters	**Type**	**Name**	**Values/Number**
Nodes	Point	POI1[(a)]	708469
Linear elements	Cube/Tetrahedra	CUB8/TET4[(a)]	489852
Accuracy	fixed point	$\lvert T_{\mathrm{n}} - T\left(\phi\left(T_{\mathrm{n}}\right)\right)\rvert \leq \epsilon_{\mathrm{pf}}$	$\epsilon_{\mathrm{pf}} = 0.01$
Convergence	Series	$\lvert T_{\mathrm{n}} - T_{\mathrm{n\text{-}1}}\rvert$	20-50 steps
Computational time	-	-	12 h.

[(a)] Cast3M notations.

Table 2.2: Map of the first and second stage of the cryo-refrigerator PT415 commercialized by Cryomech, Inc. [1]. The table gives the temperature [K] of the first and second stage as a function of their respective loads [W].

First stage					
Q_2 \ Q_1	0	21	42	63	83
0	31.5[(a)]	34.5	40	51	66
0.5	31.8	34.8	40.3	51.3	66.3
1	32	35	40.7	51.7	66.7
1.5	32.2	35.2	41	52	67
2	32.5	35.5	41.3	52.3	67.3
2.5	32.8	35.8	41.7	52.7	67.7
3	33	36	42	53	68
Second stage					
Q_2 \ Q_1	0	21	42	63	84
0	2.8	2.8	2.8	3.3	3.7
0.5	3.4	3.4	3.4	3.7	4.2
1	3.9	3.9	3.9	4.1	4.6
1.5	4.3	4.3	4.3	4.5	4.7
2	4.6	4.6	4.6	4.7	5
2.5	5	5	5	5.05	5.1
3	5.25	5.25	5.25	5.25	5.25

[(a)] The values of red color have been slightly modified compared to the original data to facilitate the convergence of the simulation.

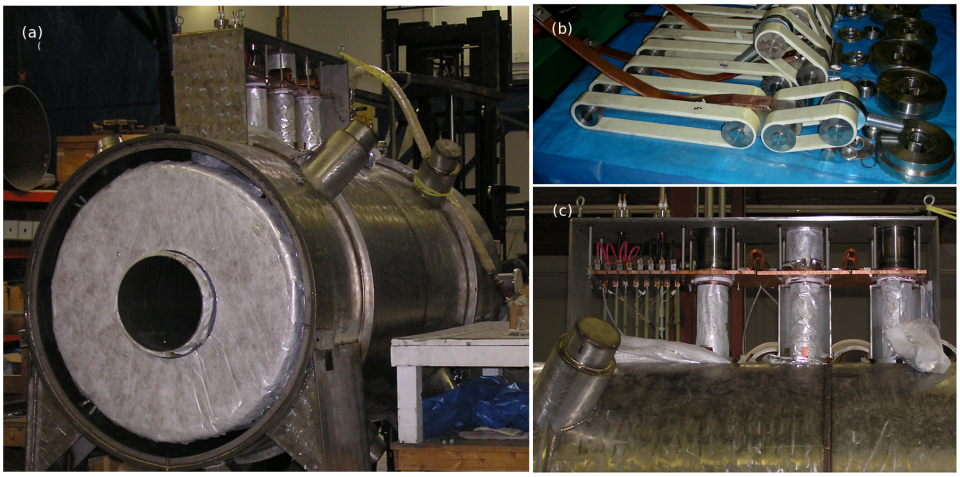

(a) Pictures of the spectrometer #1 taken at WangNMR, Inc. during its assembly in 2008.

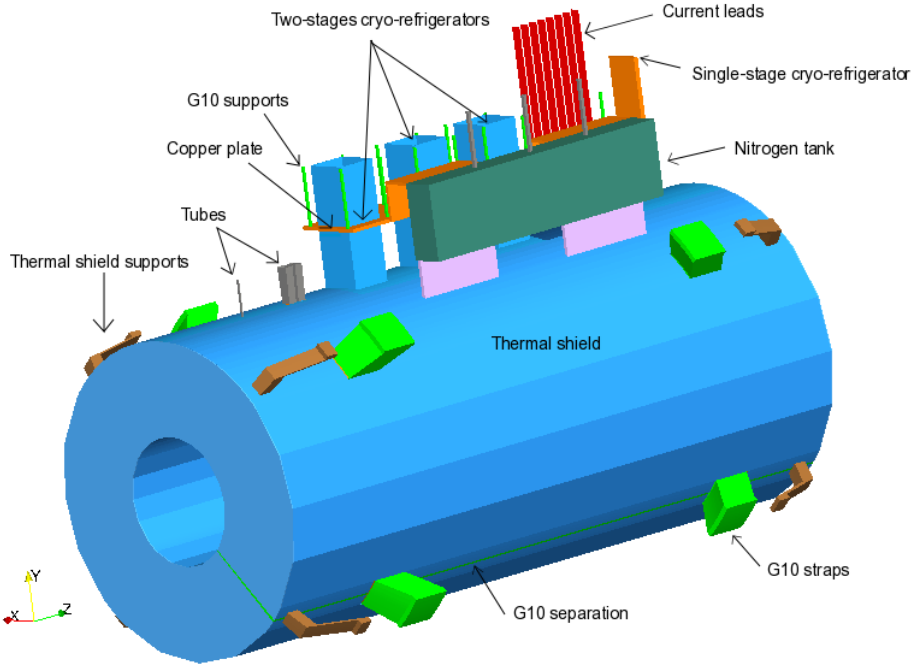

(b) Geometrical model of the spectrometer #1.

Figure 2.1: Comparision between a picture of one of the spectrometers built at WangNMR, Inc. and the geometrical model used to simulate the behavior of the cryogenic system. The pictures show: (a), the entire system; (b) the G10 straps to support the magnets within the helium vessel; (c), the copper plate supporting the first stage of the cryo-refrigerators and the current leads.

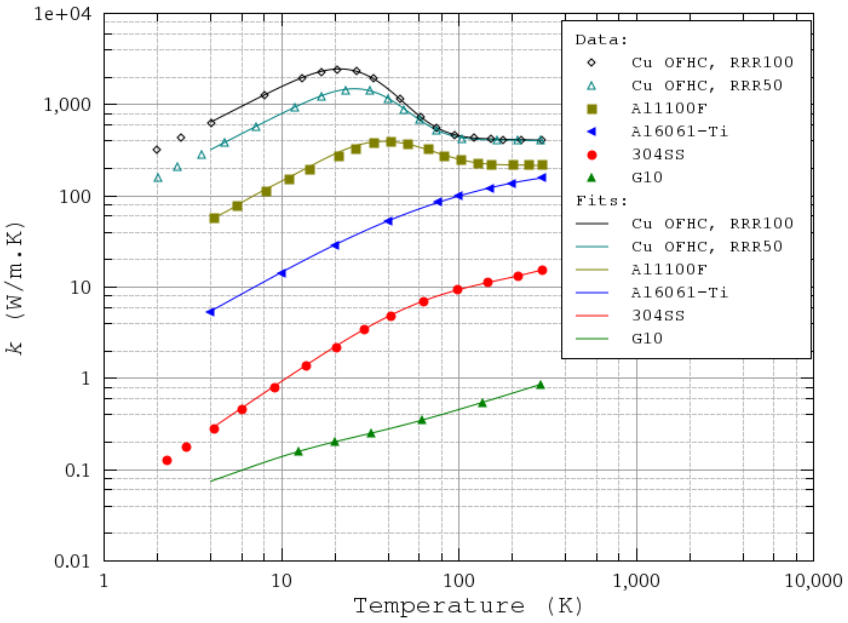

(a) Thermal Conductivity.

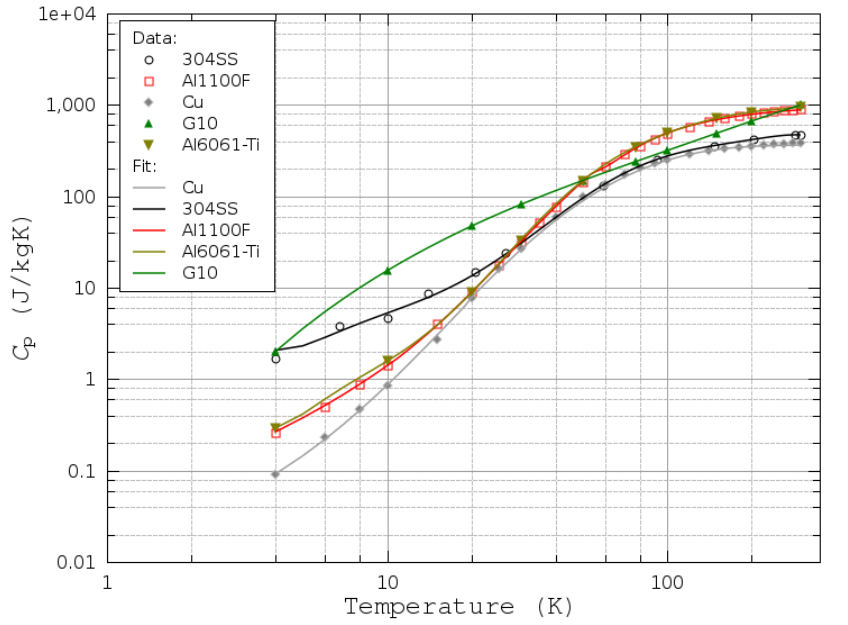

(b) Specific heat capacity.

Figure 2.2: Comparision between data from literature and fits to describe the evolution of the thermal conductivity and heat capacity of solids as a function of temperature.

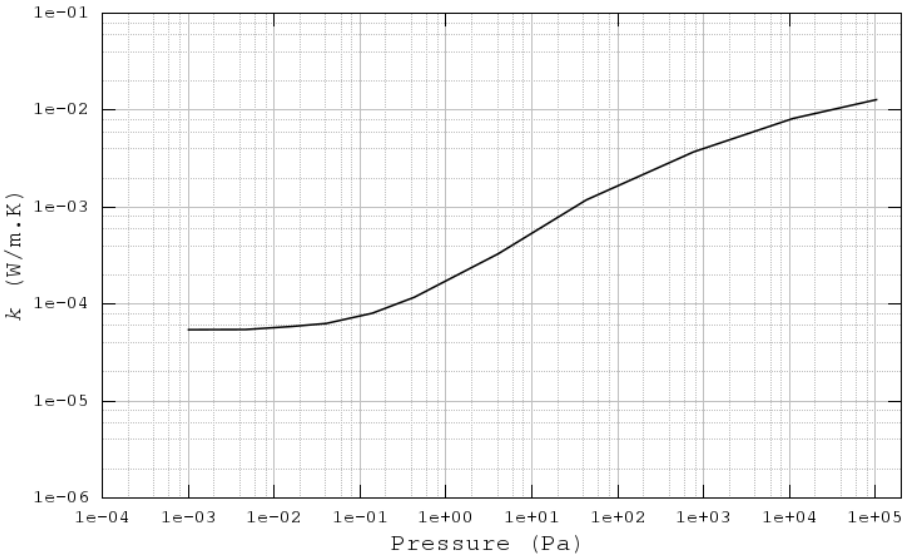

Figure 2.3: Mean thermal conductivity of super-insulation made of Aluminum foils plus fiberglass paper [2].

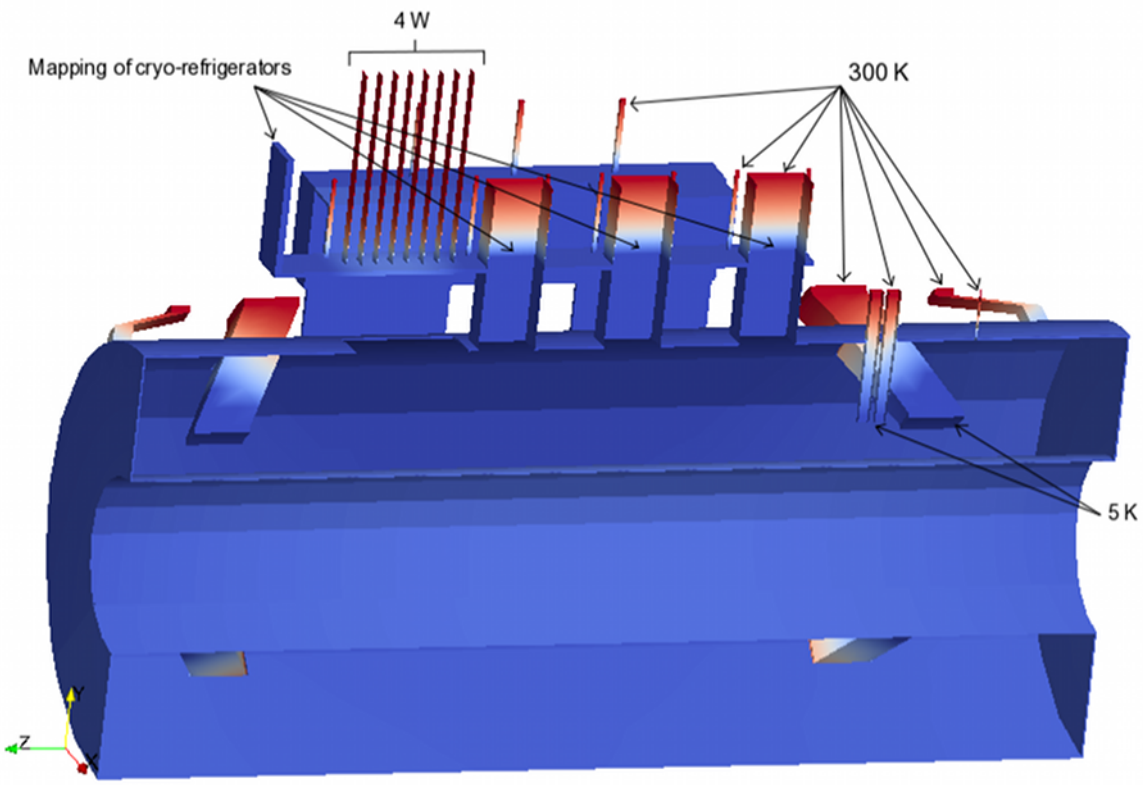

Figure 2.4: Location, type and value of boundary conditions. The mapping of cryo-refrigerators refers to the correlation between the heat load at the stages and their temperature. The current leads receive 4 W from the surrounding to match the temperature of the warm side to about 300 K.

Chapter 3

Parametric study

This chapter presents a parametric study of MICE spectrometer [1]. It focuses on the cryogenic system and its response to loads. The following work has been conducted:

- ◊ optimal number of cryo-refrigerators,
- ◊ influence of copper quality on the temperature distribution of the copper plate,
- ◊ influence of the upper current lead dissipation and design on the temperature distribution of the copper plate,
- ◊ influence of the thermal shield material on the peak temperature,
- ◊ influence of the choice of cryo-refrigerator enclosure material on the temperature distribution,
- ◊ influence of the nitrogen tank presence on the heat load at the cryo-refrigerators.

The nitrogen tank is not considered during most of the parametric studies described above. It is introduced at the very last.

3.1 Optimal number of cryo-refrigerators

During the first magnet tests, the HTS lead located at the very end of the copper plate burnt. Figure 3.1 (page 28) shows the assembly at the time of the test. A simplified model of the copper plate has been elaborated to study the influence of various parameters. It is given in figure 3.2 (page 28) [2]. The current leads

[1] It is not intended to give values reproducing the actual measurements since details of the design and imperfections are not taken into account. Trends, influences and design improvments are the authors' goals.

[2] At the time of this computation, an even simpler model was used where the current leads were reduced to a volumetric heat dissipation taking place within the copper plate. Nevertheless, the following model is presented and have been used for the rest of the study without impairing the results obtained in this section.

were represented as a volume included into the plate in which a volumetric heat dissipation was taking place.
Due to the choice of the design, the temperature profile across the copper plate with only three cryo-refrigerators does not ensure an appropriate cooling of the copper leads. Figure 3.3 (page 29) shows a simulation indicating the relevance of a better distribution of the thermal sinks [3]. The two-stage cryo-refrigerators appear as missing data in the plots. The single-stage cryo-refrigerator is located at the tip of the copper plate corresponding to the lowest temperature since it has the largest cooling power (see figure 3.2, page 28).
It would appear at first glance that only 3 cryo-refrigerators are needed. However, as the maximum cooling power of the second stage is of the order of 1.5 W per cryo-refrigerator at 4.2 K, it may not be sufficient to recondense the liquid helium boiling at a maximum rate of 2.4 L/hr corresponding to 1.6 W and the thermal loads by radiation and conduction [4]. This issue is not further discussed in this report. However, additional two-stage cryo-refrigerators might be necessary to recondense the helium vapors to meet the load requirements.

3.2 Copper plate

In this section, the influence of the quality of the copper plate is discussed. Based on the model used in the previous section, different qualities of copper material have been studied. Figure 3.4 (page 29) gives the resulting temperature profiles. The total dissipation is equal to 144 W.
Table 3.1 (page 26) gives a summary of the influence of the copper quality defined by its Residual Resistivity Ratio (RRR). The difference between the temperature profiles tends to vanish with an increasing copper quality. OFHC copper having a residual resistivity ratio greater than a few hundreds is sufficient to obtain the highest thermal redistribution across the copper plate. However, the peak temperatures span very little which do not suggest to use the highest quality to remain cost effective.

3.3 Copper current leads

Figure 3.5 (page 30) shows the influence of length of the copper current lead on the temperature profile across the copper plate. The peak temperature values are summarized in table 3.2 (page 26).
According to the model, it appears that a short length is a better choice for a given cross-section [5]. It is such because of the large cooling capacity of the cumulated

[3] Plots generated with Paraview [6]

[4] Private communication: Steve Virostek SVirostek@lbl.gov.

[5] In reality, the cooling power is limited and higher heat loads arising from the imperfections of the construction may lead to overload the cryo-refrigerators. Therefore, an optimum value should be found.

four cryo-refrigerators. However, it must be recalled that the model is an ideal case and the results must be assessed with care. The copper leads are connected to the copper plate and are extended by HTS current leads. An analytical model is performed in appendix D (page 55) which can be used to give more insight into the issues related to their implementations.

3.4 Influence of the thermal shield material

The following materials have been studied:

- ◊ OFHC copper, with a residual resistivity ratio equal to 50,
- ◊ OFHC copper, with a residual resistivity ratio equal to 1000,
- ◊ pure aluminum, Al1100F,
- ◊ aluminum alloy, Al6061-Ti (actual design).

Figure 3.6 (page 31) shows the resulting temperature profile for each case. The peak temperature is the greatest for Al6061-Ti having the smallest thermal conductivity as depicted in figure 2.2(a) (page 19). A thermal shield made of low graded copper appears as a better choice in terms of cost and temperature gradient compared to the current choice. Table 3.3 (page 26) summarizes the peak temperatures.

3.5 Influence of the cryo-refrigerator enclosure material

The same set of materials introduced in the previous section has been considered. The enclosures connect the thermal shield to the copper plate supporting the first stage of the cryo-refrigerators. They are constituted of two parts:

- ◊ the actual enclosure,
- ◊ Al1100F straps to allow flexibity.

The straps are not considered as part of the system and remain made of Al1100F throughout the study. Figure 3.7 (page 32) shows the influence of the material choice. Copper appears to be a better choice for the same reasons stated in the previous analysis. Table 3.3 (page 26) summarizes the peak temperatures.

3.6 Presence of nitrogen tank

Table 3.4 (page 27) shows the influence of the nitrogen tank on the thermal load at the first stage of cryo-refrigerators. The computation assumed an empty tank initially at 300 K. The tank if not filled with liquid nitrogen is expected to count for an extra load larger than 14 W. It is therefore recommended to whether keep the

reservoir full or to take into account this possible extra load early on in the design [6]. It is also possible to remove the tank altogether increasing the cooling time of the thermal shield.

3.7 Summary of heat loads

Table 3.5 (page 27) summarizes some of the thermal heat loads. Only the main heat loads are given. The thermal conduction through the G10 straps was analytically computed (see appendix C, page 51).

[6] The author is inclined to believe that disconnecting the tank from the first stage of the cryo-refrigerators and keeping it full may be considered as an alternative solution in the current design.

Table 3.1: Influence of OFHC copper plate quality.

RRR	**Peak temperature (K)**
50	66
100	65.3
500	64.8
1000	64.7

Table 3.2: Influence of the copper current lead length on the temperature profile of the copper plate assuming a current lead radius equal to 0.0027 m.

Length (m)	**Peak temperature (K)**
0.3	63
0.4	65.4
0.5	70

Table 3.3: Values of peak temperature as a function of constituting material.

Thermal shield		**Cryocooler enclosure**
Material	**Peak temperature (K)**	**Peak temperature (K)**
OFHC copper, RRR 100	86.6	54.5
OFHC copper, RRR 50	87.1	55
Al1100F	89.1	62
Al6061-Ti	92.4	72.5

Table 3.4: Influence of the nitrogen tank on the load at the first stage of the cryo-refrigerators.

Cryo-refrigerators	**Load without tank (W)**	**Load with warm tank (W)**
1	46	55
2	45	50
3	56	64
4	54	46
Total load (W)	201	215

Table 3.5: Summary of thermal heat loads.

Heat loads	**Value from model (W)**	**Analytical values (W)**
Radiation (thermal shield)	12	30 [11]
OFHC copper current leads (diameter equal to 0.0027 m)	24	11.3 [11]
Conduction (OFHC copper current leads, I_t = 0 A)	4	5.6
Conduction (G10 straps to thermal shield)	0.23	-

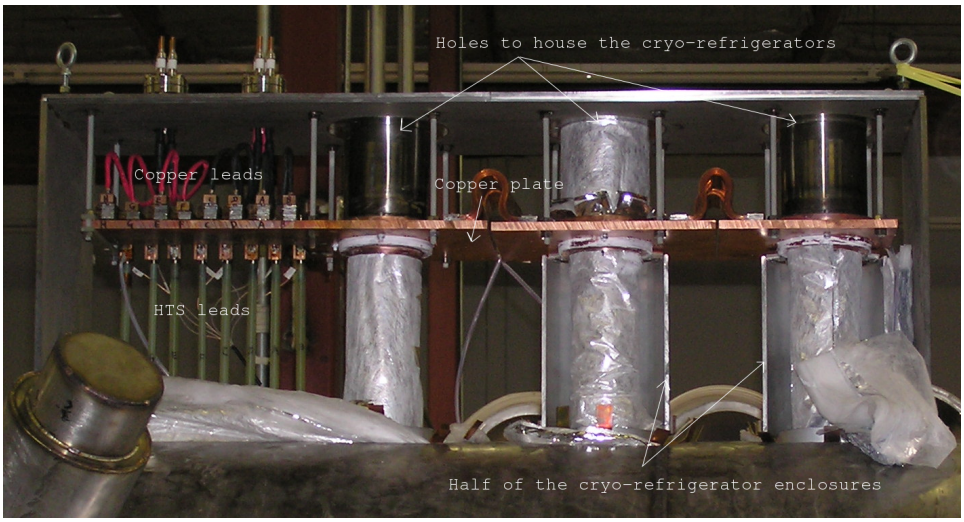

Figure 3.1: Picture of the current leads and the copper plate supporting the first stage of the cryo-refrigerators during assembly phase at WangNMR, Inc. in 2008.

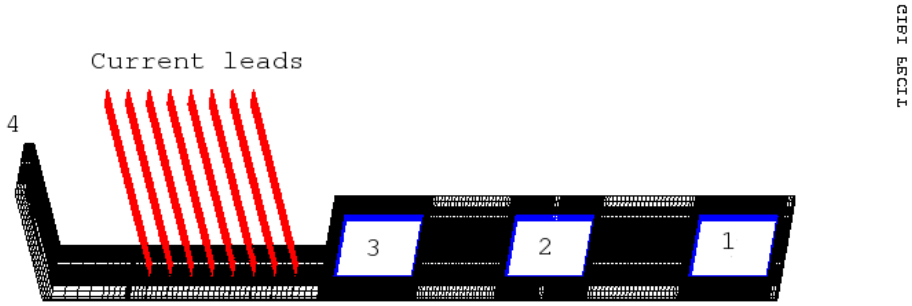

Figure 3.2: Mesh generated by Gibi, the pre- and post-processor of Cast3M. It has been used to study the influence of parameters on the copper plate. The numbers identify the cryo-refrigerators. The fourth one corresponds to the single-stage cryo-refrigerator.

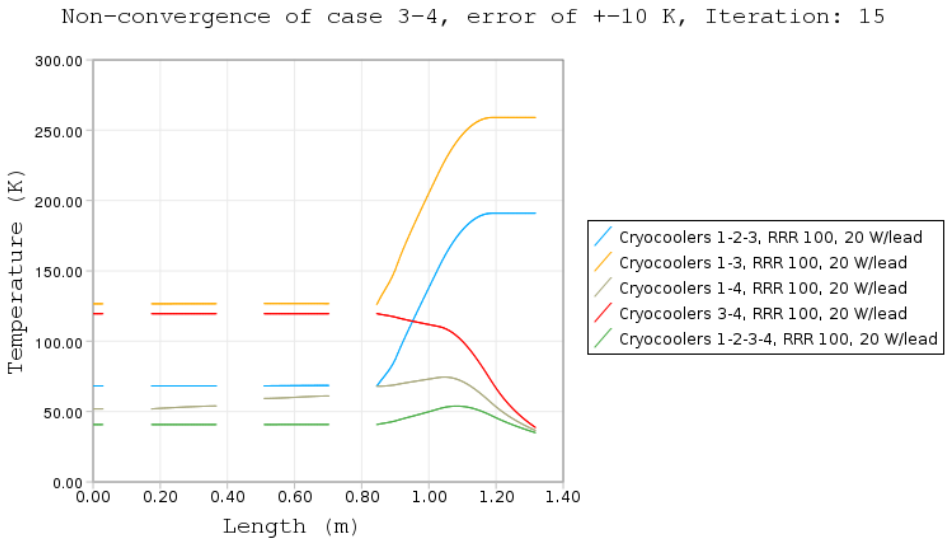

Figure 3.3: Influence of the distribution and number of cryo-refrigerators on the temperature profile across the copper plate. The system was reduced to the copper plate and the copper current leads dissipating 20 W per leads. The warm side of the leads were at a fixed temperature of 300 K.

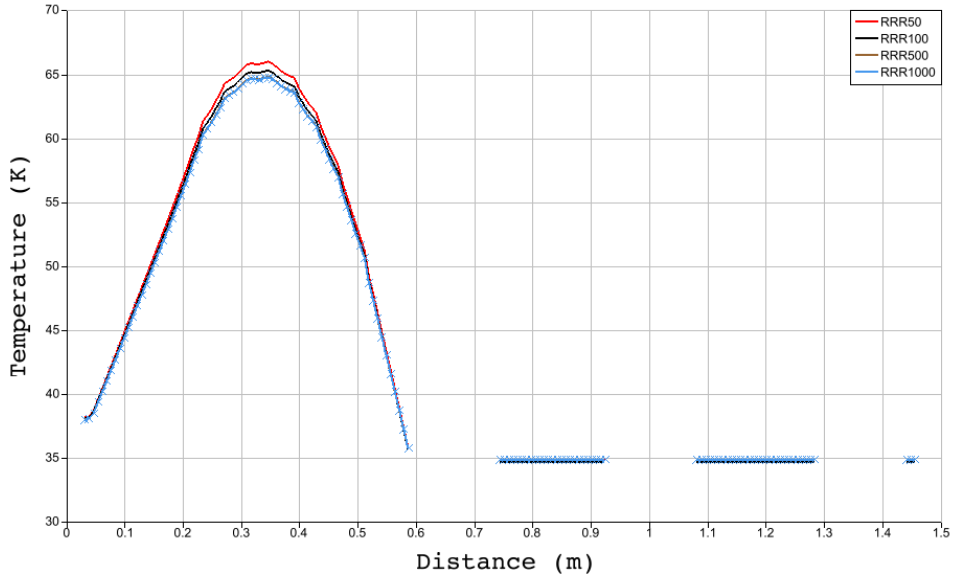

Figure 3.4: Influence of the quality of the copper plate on the temperature profile across it. The current leads dissipate 24 W with the warm side at a fixed temperature equal to 300 K.

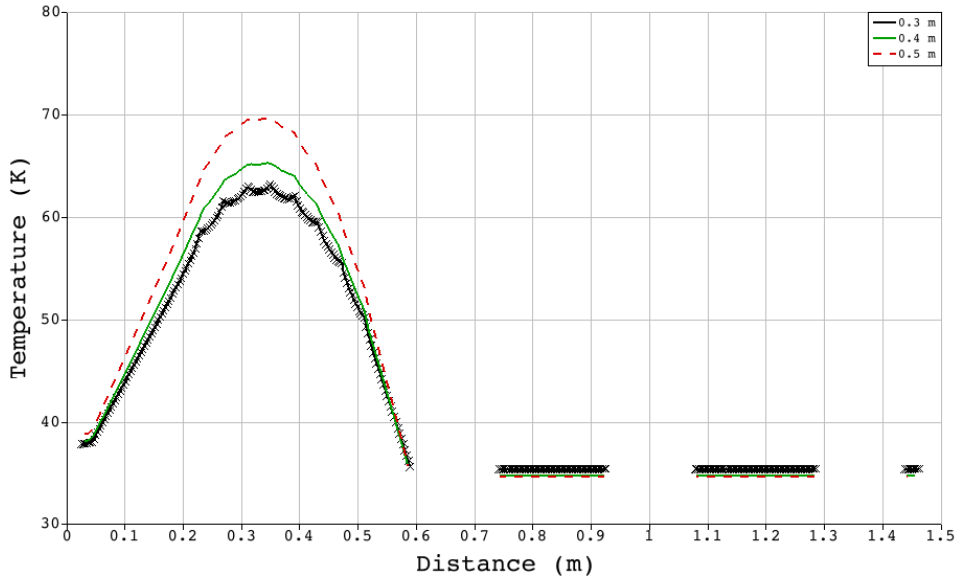

Figure 3.5: Dependence of the temperature profile across the copper plate as a function of the current lead design. The copper quality of the current leads corresponds to a residual resistivity ratio equal to 100. The warm side of the current leads is kept at a fixed temperature equal to 300 K.

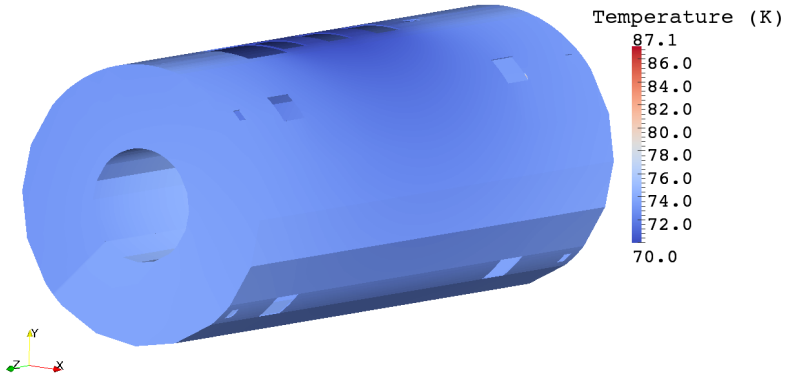

(a) Copper OFHC copper, RRR 50.

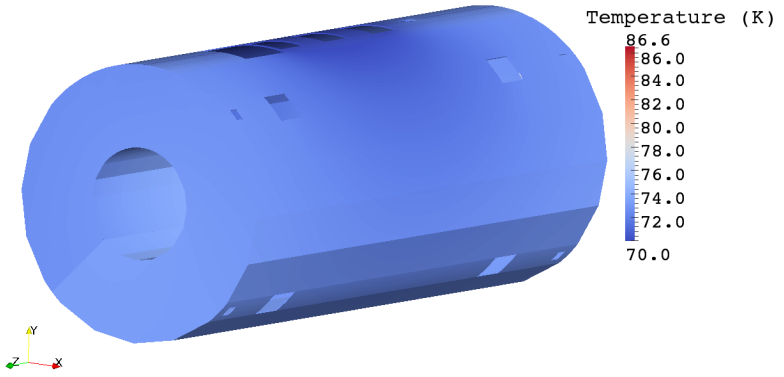

(b) Copper OFHC copper, RRR 100.

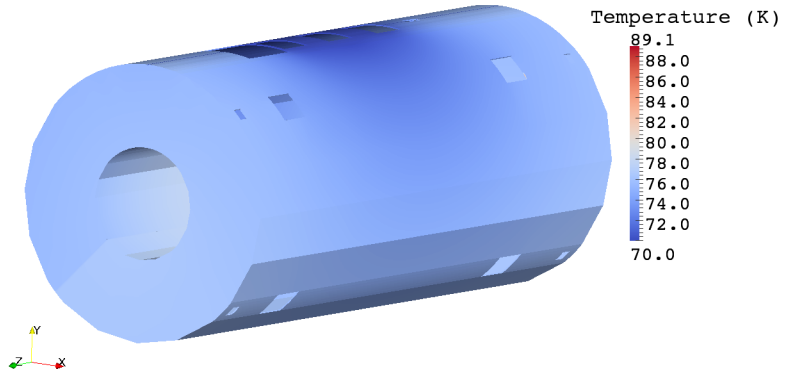

(c) Al1100F, pure.

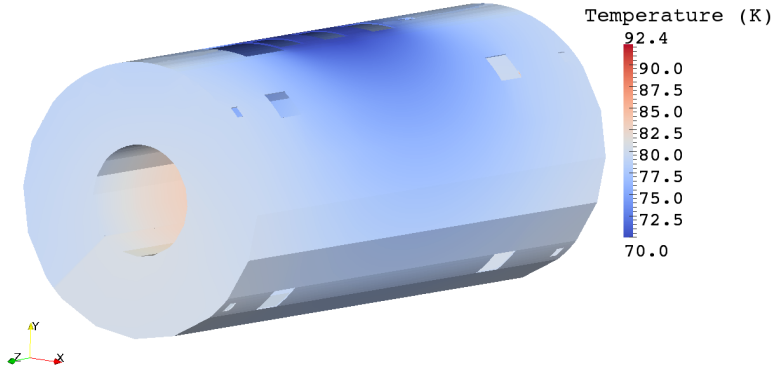

(d) Al6061-Ti, alloy.

Figure 3.6: Comparision of the temperature profile of the thermal shield for different choice of materials.

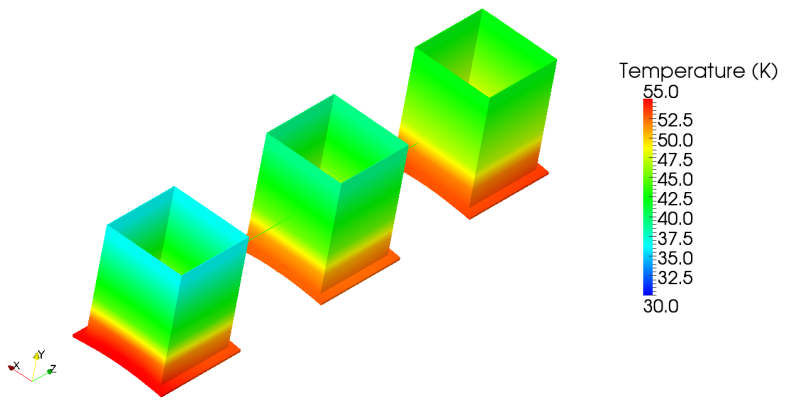

(a) OFHC copper, RRR 50.

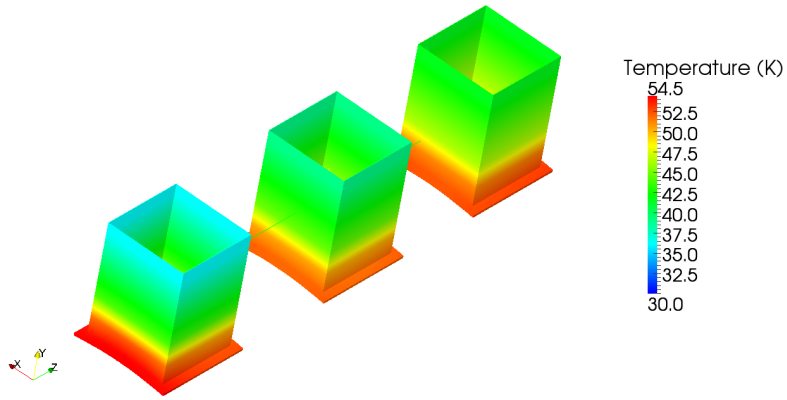

(b) OFHC copper, RRR 100.

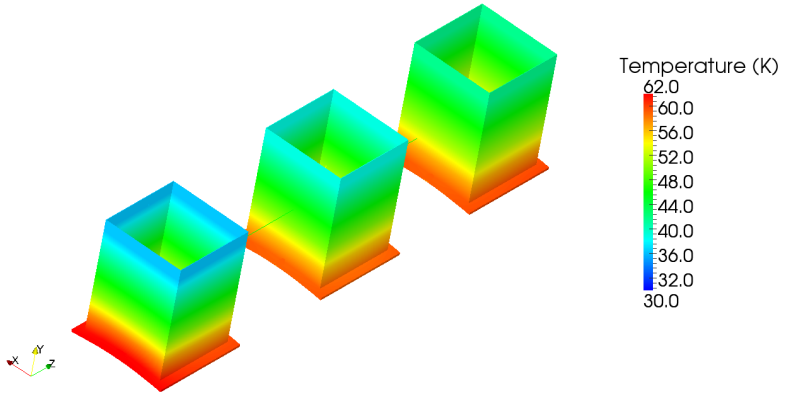

(c) Al1100F, pure.

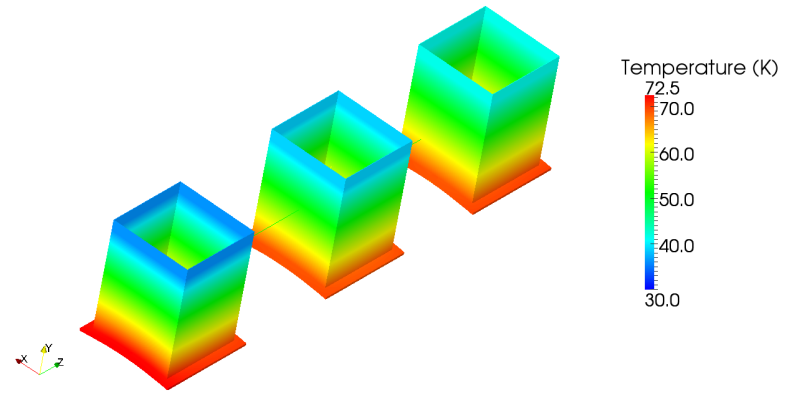

(d) Al6061-Ti, alloy.

Figure 3.7: Comparision of the temperature profile of the cryo-refrigerator enclosure for different choice of materials.

Chapter 4

Electrical and magnetic studies

The following chapter presents calculations performed on some electrical and magnetic aspects of MICE spectrometer. It does not necessary match any actual tests. The cases studied hereinafter are hypothetical magnet tests.

4.1 Parameters of the coils

Figure 4.1 (page 38) shows the model of the tracker solenoid cold mass, including the coils and insulation. The insulation on the flat sides of the coils have not been modeled. Table 4.1 (page 35) summarizes the dimensions of the solenoids. Table 4.2 (page 35) recalls their electrical parameters as described in reference [4].

4.2 Inductance of the spectrometer

Table 4.3 (page 35) compiles the estimated values of inductances. A C code, modified and recompiled by the author, has been used to perform the computations [12]. The results have been compared to an independent code [13]. Table 4.4 (page 36) shows the relative errors. A maximum error equal to 15 % has been inferred.

4.3 Stored energy and power supply ratings

Based on the previous estimated inductances, table 4.4 (page 36) has been computed. Using the power supply characteristics [4], the charging time of the solenoids have been estimated based on possible voltage-mode tests. The voltage is assumed to be set to the maximum value generated by the power supplies.

$$\begin{cases} VI = RI^2 - \mathcal{L}\dfrac{dI}{dt}, \\ \dfrac{dI}{dt} = \dfrac{V}{\mathcal{L}} e^{\dfrac{t}{\tau}}, \\ \tau = \dfrac{\mathcal{L}}{R}. \end{cases} \tag{4.1}$$

Where V is the voltage at the power supply terminals, R is the resistance of the circuitry, and $\mathcal{L}$ is its total inductance. This model does not include the protection circuit. If diodes were to be used, depending on their amount and characteristics, the charging time would be slower being determined by the actual voltage across the coils.

Table 4.1: Geometrical parameters of the coils.

Coils	**Inner radius (m)**	**Thickness (m)**	**Length (m)**	**Center position (m)**
Match 1	0.258	0.047	0.201	0.124
Match 2	0.258	0.031	0.200	0.564
End 1	0.258	0.062	0.111	0.964
Center	0.258	0.022	1.314	1.714
End 2	0.258	0.068	0.111	2.464

Table 4.2: Electric and magnetic parameters of the coils.

Coils	**Number of turns**	**Nominal current (A)**
Match 1	4830	265
Match 2	3192	286
End 1	3584	234
Center	15340	280
End 2	3968	240

Table 4.3: Inductances $[H]$.

	Match 1	**Match 2**	**End 1**	**Center**	**End 2**
Match 1	15.6	1.05	0.29	0.26	0.02
Match 2	-	6.8	0.93	0.52	0.02
End 1	-	-	13	3.2	0.05
Center	-	-	-	50	3.81
End 2	-	-	-	-	15

Table 4.4: Relative error in percent between codes of inductance calculation.

	Match 1	**Match 2**	**End 1**	**Center**	**End 2**
Match 1	10	0.6	0.5	1.9	3.3
Match 2	-	7	0.7	2.2	2.4
End 1	-	-	14	2.7	0.4
Center	-	-	-	6	3
End 2	-	-	-	-	15

Table 4.5: Stored energy $[kJ]$.

	Match 1	**Match 2**	**End 1**	**Center**	**End 2**
Match 1	547	79	18	19	1
Match 2	-	277	62	38	2
End 1	-	-	355	209	3
Center	-	-	-	1954	256
End 2	-	-	-	-	421

Table 4.6: Combination of coils. The maximum voltage and power rating of the power supplies have been assumed.

Coils	Inductance (H)	Stored energy (kJ)	Maximum voltage at power supply (V)	Power supply rating (kW)	Time constant (min.)
Match 1-Match 2	25	904	10	3	5
End 1-Center-End 2	92	3198	10	3	18
End 1-End 2	28	779	5	0.6	22
All	120	4242	10	3	24

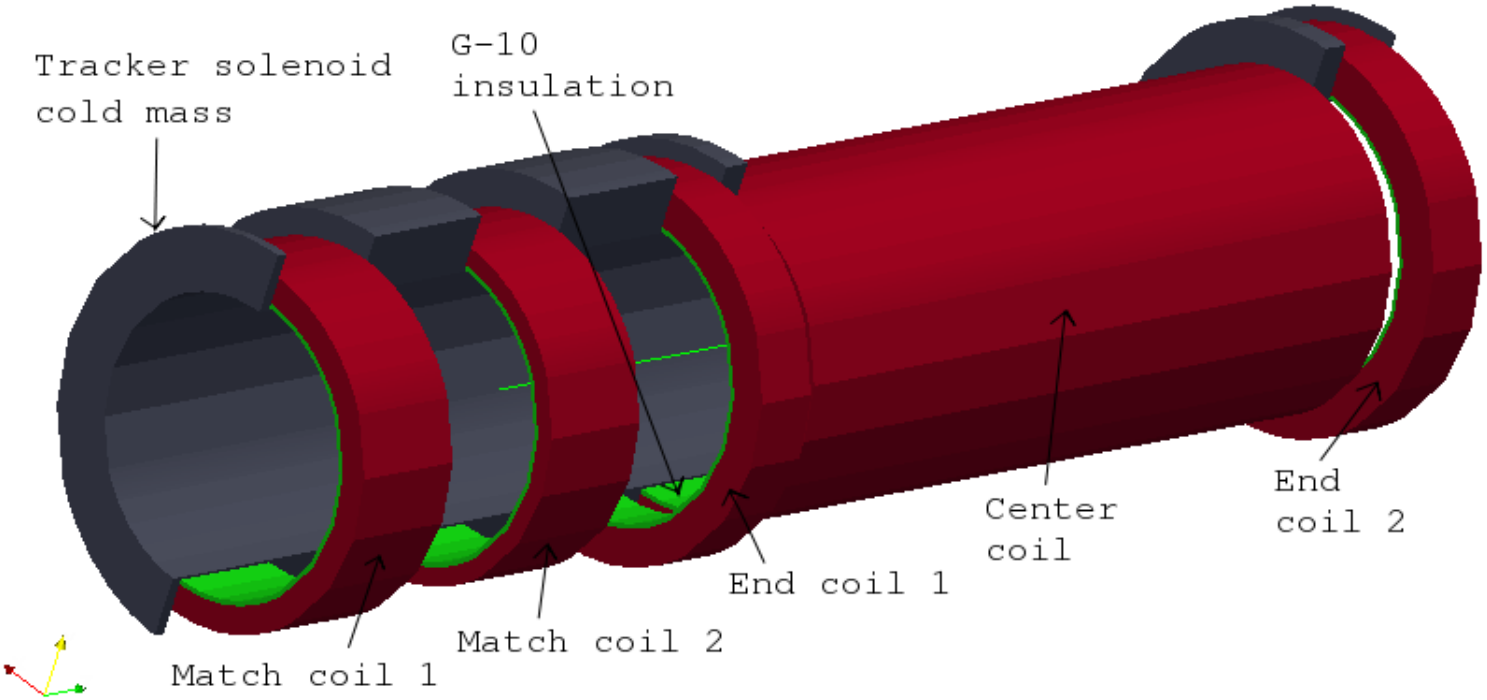

Figure 4.1: Model of the tracker solenoid cold mass and the solenoids. The magnetic computations are performed by Biot-Savart integration.

Chapter 5

Conclusion

Studies of the cooling and electrical system of MICE spectrometer have been presented. More emphasis have been given to the cryogenic system which is the critical component determining the proper operation of the spectrometer. The electrical system can be easily adjusted being external to the cryostat.
The parametric study of the system showed the relevance of a careful design of the cooling scheme. The following issues must be investigated futher [1]:

- ◊ the proper design of the copper current lead to minimize the heat load at the cold end,
- ◊ the encirclement of the current leads by the coolers,
- ◊ the quality of the thermal connections between the different parts of the system,
- ◊ the appropriate number and location of sensors,
- ◊ a clear operational procedure which corresponds to the chosen design,
- ◊ the proper choice of material and the konwledge of their properties.
- ◊ integrated quench detection and protection system with power equipments.

To minimize the peak temperature at the cold end of the copper current lead, it is necessary to equally distribute the load between the cryo-refrigerators. It is then sensible to surround the current leads. The temperature at the connection between the HTS and copper leads plays a major role in the well-been of the superconducting leads. Indeed, the superconducting properties depend on temperature, magnetic field and transport current defining a critical surface. At any point above this surface, Joule heating takes place leading to potential failure. In such an event, a perfect lead burns at about half-way along its length [14] which would not be detected by temperature sensors at the terminals. Hence, it is highly recommended to install voltage taps across the HTS leads to ensure their safe behavior. It may be used as part of the quench detection system as well.

[1] This list is not exhaustive and might be completed upon design details.

The appropriate number and type of sensors must be evaluated to track the main heat loads. In this case, the author recommands to monitor a minimum of one G10 strap and thermal shield support in addition to the current scheme.
A clear operational procedure refers to the cooling procedure. The nitrogen tank, if installed must be kept cold, to avoid unnecessary extra heat loads coming from 300 K which in addition to loading the cryo-refrigerators changes the temperature profile of the thermal shield. In view of the temperature at the copper plate, it is not recommended to connect it to the nitrogen tank or a careful design must be considered.

Large uncertainties are pertaining to the material properties. Even though data are available in the literature, it is safe to rely on measurements. Thermal conduction tests my be conducted to characterize some specific materials known to show a broad range of values such as fiberglass or uncommon alloys [2]. In the case of copper, a simple residual resitivity ratio measurement is enough to get an accurate estimation of its quality. However, it involves liquid helium to reach the plateau of residual resistivity below 30 K.

The electrical circuitry is external to the system. The detection and protection system is critical to ensure the reliability of the system. The issues related to the electrical circuitry resides in the strong coupling between the magnets which are operated by different power supplies. It suggested to study the behavior of the entire cicuitry assuming different fault conditions and to define a proper energization procedure.

Table 5.1 (page 41) attempts to summarize the above recommendations.

[2] It is not necessary to estimate the heat capacity since the systems is operated in steady state.

Table 5.1: Design issues to investigate and recommendations.

Item	Design issue	Recommendations	Criticality
Copper leads	Ratio length to cross-section area	Optimum design depends on chosen boundary conditions. A minimum of 8 W must be pulled out at the cold end.	Medium
HTS leads	Temperature at warm end	To be incorporated in copper lead design. Voltage monitoring and integration to the protection scheme.	High
Cryo-cooling scheme	Distribution of cold extraction and thermal sensors	Minimization of temperature gradients (straps, warm end of HTS leads). Any critical heat paths must be monitored (cold supports). Quality control of welds and junctions.	High
Operation	Magnet energization and cooling procedures	Clarification of magnet and cooling operation through step-by-step written procedures to be validated by all parties. They may take into account design details (nitrogen tank).	Medium
Material properties	Quantification of errors	Recommended measurements on custom-made fiberglass straps and uncommon alloys.	Medium
Electrical equipments	Design of the quench protection and detection system in conjunction of choice of power sources	Circuit design must be based on magnet characteristics. An integrated system is suitable especially for such large coupled solenoids. The magnitude of the inductance of the entire system is similar to commercial NMR magnets. It is recommended to seek external expertise from private sector. It is advised to run simulation of the entire electrical circuitry prior to operate the magnet baring in mind possible fault cases (electrical hasard and safety assessments).	Medium

Appendix A

Table referencing the different parts of MICE spectrometer

Table A (page 42) summarizes the different parts composing MICE spectrometer according to WangNMR, Inc.'s report [4].

Table A.1: Parts consituting MICE spectrometer. Identification of the parts included in the numerical model.

Parts	**Drawings reference [15]**	**Material**	**Modeled (Y/N)**
60K shield			
Outer cylinder	6100	Al6061-Ti	Y
End plate	6200	Al6061-Ti	Y
Removable cover	6300	Al6061-Ti	Y
Center cylinder	6400	Al6061-Ti	Y
Mounting plate	6510	OFHC copper	Y
Extend cylinder	6520	Al6061-Ti	Y
Bi-metal part	6530	Cu-Al	Y
Thermal bumper	6600	G-10	Y
Tracker module			
Coil form	C001	Al6061-Ti	Y

... continued on next page

... continued from previous page

LHe vessel	C002	Al6061-Ti	Y
Side insulation	C003	G-10	N
Reinforcement	C004	Al6061-Ti	Y
Suspension ring	C005	Al6061-Ti	Y
Be-metal coupling	C006	Al-SS	N
Cold mass support bracket	C007	316SS	Y
Be-metal coupling	C008	Al-SS	N
Neck tube	C009	304SS	N
Precool nozzle	C010	304SS	N
Precool line	C011	304SS	N
LHe return tube	-	SS	Y
Washer	C012	304SS	N
Condensers			
LHe condenser	CON-000	304SS/OFHC copper	N
Vacuum cylinder	CON-002	304SS	N
Vacuum disk	CON-003	304SS	N
Cryocooler installation			
-	C002	304SS	N
-	C003	304SS	N
-	C004	304SS	Y
-	C005	OFHC copper	Y
-	C006	304SS	N
-	C007	304SS	N
Vacuum vessel			
Cylinder	3110	304SS	N

... continued on next page

... continued from previous page

End flange	3120	304SS	N
Stop ring	3130	304SS	N
Reinforcement	3140	304SS	N
LHe transfer tower	3160	304SS	N
Tube	3161	304SS	N
Disc	3162	304SS	N
Vacuum seal ring	3163	304SS	N
Flange	3170	304SS	N
Back end plate	3200	304SS	N
Front end plate	3300	304SS	N
Center tube	3400	304SS	N
Cryocooler tower			
Side plate 1	3151	304SS	N
Side plate 1	3152	304SS	N
End plate	3153	304SS	N
Window	3154	304SS	N
Cover	3155	Al6061-Ti	N
Flange	3156	304SS	N
Cover	3155	Al6061-Ti	N
Cold mass support			
Support tube	3510	304SS	N
Support plate	3520	304SS	N
Vacuum seal cover	3530	304SS	N
Cryocooler mounting plate	3600A	304SS	N
LHe transfer tower			

... continued on next page

... continued from previous page

Tube	3710	304SS	N
Flange	3720	304SS	N
Cover plate	3730	304SS	N
Reinforcing plate	F002	304SS	N
Support stand			
Plate	F001	304SS	N
Square 1	F003	304SS	N
Square 2	F004	304SS	N
Square 3	F005	304SS	N
Gusset plate	F006	304SS	N
Cryoccoler mounting plate			
Sinlge stage cryocooler	M001	OFHC copper	Y
Side plate 1	M002	304SS	N
Side plate 2	M003	304SS	N
End plate	M004	304SS	N
Window frame	M005	304SS	N
Window cover	M006	304SS	N
Cooler tube	M007	304SS	N
Cooler flange	M008	304SS	N
Copper plate	M009	OFHC copper	Y
Flexible copper strip	M010	OFHC copper	Y
Plate	M011	304SS	N
LN2 reservoir			
Reservoir	-	Al1100	Y
Connection to copper plate	-	OFHC copper	Y

... continued on next page

... continued from previous page

Connection to 60K shield	-	Al6061-Ti	Y
Miscellaneous			
Thermal shield support bands	-	G-10	Y
25T cold mass support	L000	304SS/Inconel/S2-glass	Y

Appendix B

Simplification of the geometry

Lumped versus sub-geometries: For transient analysis, it is not usually possible to lump the material properties into a single model because of the discrepancy between thermal time constants of the different constituting parts. Figure B.1 (page 49) and figure B.2 (page 50) present a typical case.

The thermal shield supports are made of stainless steel and fiberglass. Combining the information given by the thermal diffusion time and the temperature profile in steady state, the G10 part whereas on the warmest side still delays the establishement of the steady regime. In this specific example, it would have been more sensible to place the G10 part on the coolest side to benefit from its lower thermal conductivity.

Adjustment of the geometrical dimensions: Even if the sub-geometries are taken into account, their actual shape and details are not necessary respected. As the entire geometry has been coded, simplifications have been made and coefficients have been introduced to correct the discrepancies. These coefficients are related to volume ratio, x_{cp} (heat capacity, C), and normalized ratio, x_{tc} (thermal conductivity, $\mathcal{K}$). They are defined as follows:

$$\begin{cases} x_{\mathrm{cp}} = \dfrac{\mathcal{V}_{\mathrm{a}}}{\mathcal{V}_{\mathrm{m}}}, \\ x_{\mathrm{tc}} = \dfrac{\mathcal{V}_{\mathrm{a}} L_{\mathrm{m}}^2}{\mathcal{V}_{\mathrm{m}} L_{\mathrm{a}}^2}. \end{cases} \tag{B.1}$$

where the volume is noted $\mathcal{V}$, and the length, L. The actual geometry and the model are identified by the following subscripts: a and m. Table B.1 (page 49) gives the fractions corresponding to the different parts constituting the thermal shield supports. These fractions are multiplied by their related material property to define equivalent properties:

$$\begin{cases} C_{\text{eq}} = x_{\text{cp}} C, \\ \mathcal{K}_{\text{eq}} = x_{\text{tc}} \mathcal{K}. \end{cases} \tag{B.2}$$

Even though this method allows to respect the first law of thermodynamics, it leads to an inaccurate temperature distribution. However, this study focuses on the capacity of the cooling system to handle the various heat loads. The inaccuracies in the thermal profile are irrelevant in this case. However, care has been taken to minimize the dimensional discrepancies between the model and the actual geometry.

Table B.1: Dimensional comparision between the actual geometry and the model for the thermal shield support.

Parts	$\mathbf{x}_{cp}$	$\mathbf{x}_{th}$
G10	0.093	0.662
Stainless steel	0.024	0.011

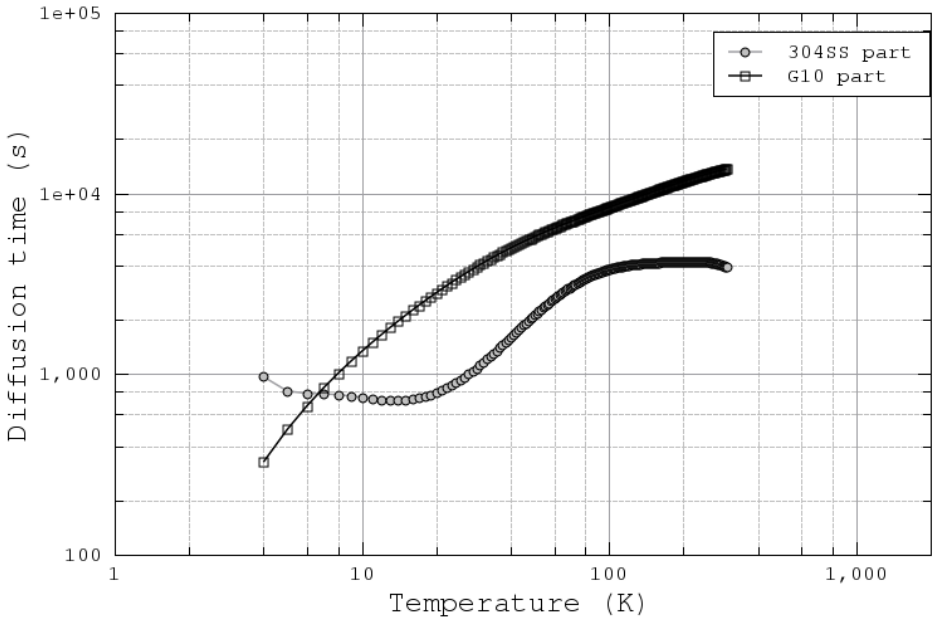

Figure B.1: Thermal diffusion time across the stainless steel and G10 parts constituting the thermal shield support.

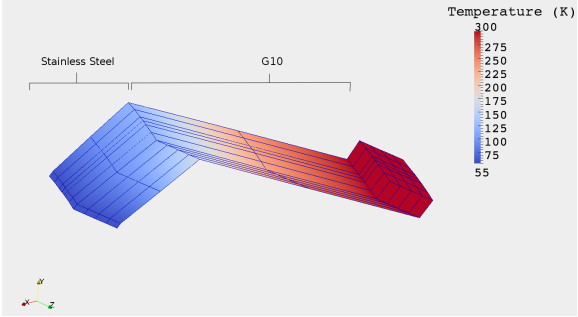

(a) Model of the thermal shield support.

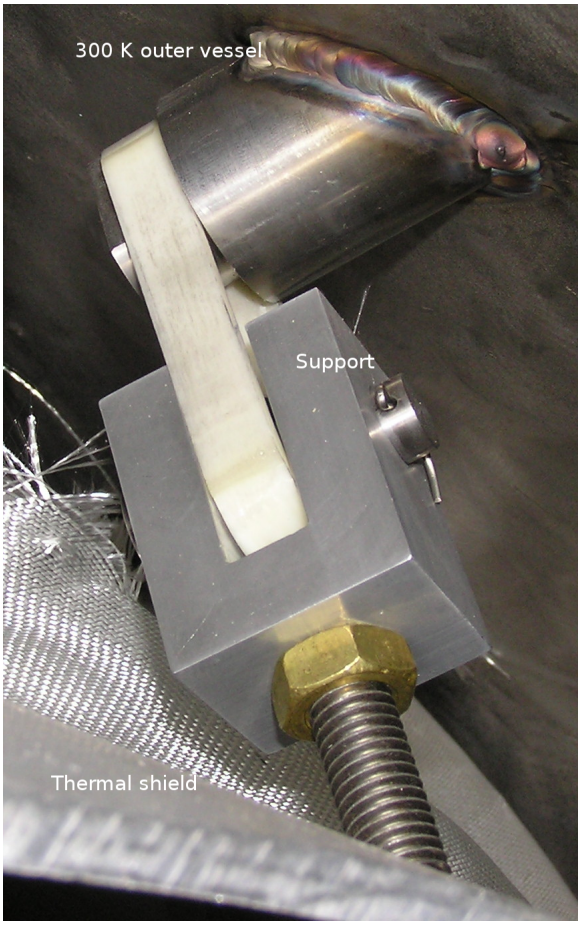

(b) Actual geometry.

Figure B.2: Actual thermal shield support and temperature distribution across the corresponding model.

Appendix C

Semi-analytical model of the cold mass supports

The following appendix presents a semi-analytical modelization of the cold mass supports. The result is compared to those obtained with FEM computation.

C.1 Assumptions

To conduct this analysis, the following assumptions have been made:

- ◊ steady state,
- ◊ idealized geometry,
- ◊ boundary conditions: fixed temperatures,
- ◊ material properties dependent on mean temperature between connections.

C.2 Semi-analytical model

The model is based on the analogy between the thermal heat balance equation and the corresponding electrical equation in steady state [1]. Based on figure C.1 (page 54), Φ is the thermal heat flux and R is the thermal resistance defined as follows:

$$\mathcal{R} = \frac{1}{\mathcal{K}_{\text{av}}} \frac{L}{A}. \tag{C.1}$$

where $\mathcal{K}_{\text{av}}$ is the mean thermal conductivity updated at each computational step:

[1] The validity of the analogy is given by the two following relations and there corresponding electrical equivalents:

$$\begin{cases} \Phi_1 = \Phi_2 + \Phi_3, & \text{conservation of current,} \\ T_{\text{i}} = \mathcal{R}_{\text{i}}\Phi_{\text{i}}, & \text{Ohm's law.} \end{cases}$$

$$\mathcal{K}_{\text{av}} = \frac{1}{(T_{\text{bc}} - T)} \int_{T}^{T_{\text{bc}}} \mathcal{K}(x)\, dx \simeq \frac{1}{2} \frac{\sum_{\text{p=1}}^{\text{n}} \left[\left(T_{\text{p}} - T_{\text{p-1}} \right) \left(\mathcal{K}_{\text{p}} - \mathcal{K}_{\text{p-1}} \right) \right]}{(T_{\text{bc}} - T)}. \tag{C.2}$$

The length and cross-sectional area are labeled L and A, respectively. Table C.1 (page 53) summarizes the corresponding entities. The temperature, T, at the intersection of the branches is solved as well as the various heat fluxes. The following equations are considered:

$$\begin{cases} T - T_1 = \mathcal{R}_1 \Phi_1, \\ T - T_2 = -\mathcal{R}_2 \Phi_2, \\ T - T_3 = -\mathcal{R}_3 \Phi_3, \\ \Phi_1 = \Phi_2 + \Phi_3. \end{cases} \tag{C.3}$$

Using a matrix representation, the following system must be solved:

$$\begin{bmatrix} 1 & -\mathcal{R}_1 & -\mathcal{R}_1 \\ 0 & -\mathcal{R}_2 & 0 \\ 0 & 0 & -\mathcal{R}_3 \end{bmatrix} \begin{bmatrix} T \\ \Phi_2 \\ \Phi_3 \end{bmatrix} = \begin{bmatrix} T_1 \\ T_2 \\ T_3 \end{bmatrix} \tag{C.4}$$

The boundary conditions T_1, T_2 and T_3 are given in table C.2 (page 53).
The inversion of the system leads to [2]:

$$\begin{bmatrix} T \\ \Phi_2 \\ \Phi_3 \end{bmatrix} = \begin{bmatrix} 1 & \frac{\mathcal{R}_1}{\mathcal{R}_2} & \frac{\mathcal{R}_1}{\mathcal{R}_2 (\mathcal{R}_1 + \mathcal{R}_3) + \mathcal{R}_1 \mathcal{R}_3} \\ 0 & \frac{1}{\mathcal{R}_2} & \frac{\mathcal{R}_3}{\mathcal{R}_2 [\mathcal{R}_2 (\mathcal{R}_1 + \mathcal{R}_3) + \mathcal{R}_1 \mathcal{R}_3]} \\ 0 & 0 & \frac{1}{\mathcal{R}_2 (\mathcal{R}_1 + \mathcal{R}_3) + \mathcal{R}_1 \mathcal{R}_3} \end{bmatrix} \begin{bmatrix} T_1 \\ T_2 - T_3 \\ \mathcal{R}_2 (T_3 - T_1) + \mathcal{R}_1 (T_3 - T_2) \end{bmatrix} \tag{C.5}$$

Table C.3 (page 53) gives the results obtained when the boundary conditions match those of Cast3M [3]. The temperature shows a good agreement with a relative error inferior to 1.2 %. The appendix F (page 65) presents the C++ routine used to solve the semi-analytical model.

[2] $det(A) = (\mathcal{R}_1 + \mathcal{R}_2) \left[(\mathcal{R}_1 + \mathcal{R}_2)(\mathcal{R}_1 + \mathcal{R}_3) - \mathcal{R}_1^2 \right] > 0.$

[3] The heat fluxes were only computed for the semi-analytical code.

Table C.1: Analogy between thermal and electrical entities.

Thermic	**Electric**	**Physical law**
Φ (W)	I (A)	Kirchhoff's current law
T (K)	V (V)	Kirchhoff's voltage law
$\mathcal{R}$ (K/W)	R (Ω)	Linearization/Ohm's law

Table C.2: Values of the boundary conditions.

Boundary conditions	**Values (K)**
T_1	300
T_2	5
T_3	84[(a)]

[(a)] Average temperature obtained with Cast3M.

Table C.3: Results of the semi-analytical computation.

Degree of freedom	**Results**	**Cast3M's results**	**Relative error**
T	85 K	86 K	1.2 %
Φ_1	0.38 W	-	-
Φ_2	0.12 W	-	-
Φ_3	0.26 W	-	-

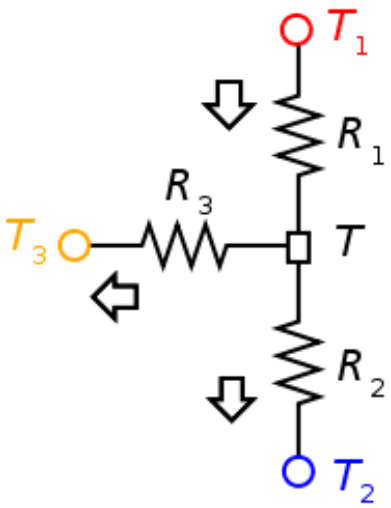

Figure C.1: Schematic drawing of the G10 straps (labeled 1 and 2) and its thermal intercept (label 3). The arrows give the presumed directions of the fluxes.

Appendix D

Analytical model of the system: copper and HTS current leads

D.1 Analytical model and assumptions

Figure D.1 60 shows the schematic drawing on which the following assumptions are based:

- ◊ steady state,
- ◊ boundary conditions: fixed temperatures,
- ◊ material properties dependent on mean temperature,
- ◊ idealized geometry,
- ◊ steady state current sharing over the entire HTS lead.

This last assumption corresponds to an unlikely scenario. Typical quenches occur locally at mid-way of the HTS lead or unusually at the extremities. A local and sharp heat spot is expected which may lead to partial melting of the superconducting tape [16].

D.2 Mathematical model

Based on the above assumptions, the following system of equations must be solved:

$$\begin{cases} \dfrac{dT^2}{d^2z} + \dfrac{\rho_1}{\mathcal{K}_1} J_1^2 = 0, \ \forall z \in [0, z_1]\,, \\ \dfrac{dT^2}{d^2z} + \dfrac{\rho_2}{\mathcal{K}_2} J_2^2 = 0, \ \forall z \in [z_1, z_2]\,. \end{cases} \tag{D.1}$$

with,

$$\begin{cases} \dfrac{\rho_1}{\mathcal{K}_1} \simeq a_1 \left(T - T_{\mathrm{r}1}\right) + b_1, \\ \dfrac{\rho_2}{\mathcal{K}_2} \simeq a_2 \left(T - T_{\mathrm{r}2}\right) + b_2, \end{cases} \tag{D.2}$$

where ρ_1 and ρ_2 are the electrical resistivities of OFHC copper and 11%Au-Ag (resitive matrix of HTS current leads), respectively. $\mathcal{K}_1$ and $\mathcal{K}_2$ are the respective thermal conductivities. The current densities and the lengths of the leads are annotated by J and z_1, z_2. Those equations are coupled by their boundary conditions. At the connection between the leads and the copper plate, the heat flux is conserved according to the first law of thermodynamics:

$$\Phi_1 = \Phi_2 + \Phi_3. \tag{D.3}$$

The heat flux Φ_3 follows the load map of the cryo-refrigerators. The author assumed a perfect connection to a two-stage cryo-refrigerator with its second stage fully loaded at 1.5 W. The following linear relation has been derived [1]:

$$\Phi_3 \simeq p_0 + p_1 T. \tag{D.4}$$

The generic solutions of the system of equations D.1 are as follows:

$$\begin{cases} T\left(z\right) = T_{\mathrm{r}1} + \dfrac{F_1}{\omega_1^2} + a\cos\left(\omega_1 z\right) + b\sin\left(\omega_1 z\right), \ \forall z \in \left[0, z_1\right], \\ T\left(z\right) = T_{\mathrm{r}2} - \dfrac{F_2}{\omega_2^2} + ce^{\omega_2 (z - z_1)} + de^{-\omega_2 (z - z_1)}, \ \forall z \in \left[z_1, z_2\right]. \end{cases} \tag{D.5}$$

where a, b, c and d are constants of integration, and:

$$\begin{cases} F_1 = -b_1 J_1^2, \\ F_2 = -b_2 J_2^2, \\ \omega_1 = \sqrt{|a_1|} J_1, \\ \omega_2 = \sqrt{|a_2|} J_2. \end{cases}$$

Additional variables are introduced to simplify the algebra:

[1] The same calculation can be refined using a quadratic fit and a resistive term to take into account a possible thermal gradient between the connection and the refrigerator.

$$
\begin{cases}
\beta = \dfrac{\mathcal{K}_1 A_1 \omega_1}{\mathcal{K}_2 A_2 \omega_2}, \\
e_1 = \left(T_{\mathrm{r}1} + \dfrac{F_1}{\omega_1^2}\right) - \left(T_{\mathrm{r}2} - \dfrac{F_2}{\omega_2^2}\right) + a\cos\left(\omega_1 z_1\right), \\
e_2 = \beta \sin\left(\omega_1 z_1\right) a - \left[\dfrac{p_0 + \left(T_{\mathrm{r}2} - \dfrac{F_2}{\omega_2^2}\right) p_1}{\mathcal{K}_2 A_2 \omega_2}\right], \\
e_3 = T_2 - T_{\mathrm{r}2} + \dfrac{F_2}{\omega_2^2}, \\
g_1 = \left[\dfrac{\beta e_1 + \tan\left(\omega_1 z_1\right) e_2}{\beta + \left(\dfrac{p_1}{\mathcal{K}_2 A_2 \omega_2} - 1\right)\tan\left(\omega_1 z_1\right)}\right] - e_3 \mathrm{e}^{-\omega_2 (z_2 - z_1)}, \\
g_2 = \left[\dfrac{\beta + \left(\dfrac{p_1}{\mathcal{K}_2 A_2 \omega_2} + 1\right)\tan\left(\omega_1 z_1\right)}{\beta + \left(\dfrac{p_1}{\mathcal{K}_2 A_2 \omega_2} - 1\right)\tan\left(\omega_1 z_1\right)}\right] - \mathrm{e}^{(-2\omega_2 (z_2 - z_1))}.
\end{cases}
\tag{D.6}
$$

The constants are given hereinafter:

$$
\begin{cases}
a = T_1 - T_{\mathrm{r}1} - \dfrac{F_1}{\omega_1^2}, \\
b = \dfrac{c + d - e_1}{\sin\left(\omega_1 z_1\right)}, \\
c = \left[\left(\dfrac{\beta e_1 + \tan\left(\omega_1 z_1\right) e_2}{\beta + \left(\dfrac{p_1}{\mathcal{K}_2 A_2 \omega_2} - 1\right)\tan\left(\omega_1 z_1\right)}\right) - \left(\dfrac{\beta + \left(\dfrac{p_1}{\mathcal{K}_2 A_2 \omega_2} + 1\right)\tan\left(\omega_1 z_1\right)}{\beta + \left(\dfrac{p_1}{\mathcal{K}_2 A_2 \omega_2} - 1\right)\tan\left(\omega_1 z_1\right)}\right)\right] d, \\
d = \dfrac{g_2}{g_1}.
\end{cases}
\tag{D.7}
$$

Table D.1 59 summarizes the parameters. Figure D.2 60 gives various temperature profiles obtained at different percentages of transport current which flows trhough the resitive matrix of the superconducting current lead in steady state. Table D.2 59 compiles the temperatures obtained at the connection for the various

cases. It is assumed that the HTS tape undergoes a quench over its entire length [2]. The temperature at the connection remains within bonds that ensures a proper functioning of the HTS current leads. Nevertheless, it must be noted that the temperature at the connection with the copper plate is weakly dependent on the dissipation occuring within the superconducting lead. A sensitivity, defined as the variation of the temperature at the connection as a function of current in the HTS matrix, was estimated equal to 0.63 K/W. Base on this result, it is recommended to add voltage taps across the HTS current leads in case they transit to a normal resistive state [3].

The C code listing is given in appendix F (page 65).

[2] This assumption is limiting since a transient quench model would be more realistic. However, such complicated approach is beyond the scope of this technical note and would not give more information to this particular study.

[3] Considering a more realistic case with a local heat spot within the HTS lead would support further the necessity of installing voltage taps across the HTS leads.

Table D.1: Parameters of the analytical model.

Parameters	**Value**
OFHC copper (RRR 100)	
Length, z_1 [m]	0.4
Area, A_1 [m^2]	22e-6
Slope, a_1 [Ωm^{2}K/W]	1.757×10^{-13}
b_1 [Ωm^{2}K^2/W]	6.57e-13
Reference temperature, T_{r1} [K]	50
11%AuAg (HTS lead datasheet [17])	
Length, z_2 [m]	0.29
Area, A_2 [m^2]	8×10^{-7} [14]
Slope, a_2 [Ωm^{2}K/W]	-2×10^{-12}
b_2 [Ωm^{2}K^2/W]	6.5e-10
Reference temperature, T_{r2} [K]	50
Linear fit: $\Phi_3 \simeq \Phi_3\,(4.3\ K, T)$	
p_0, [W]	-59.5
p_1, [W/K]	2.236

Table D.2: Temperature at the connection of the copper and 11%AuAg HTS leads. A transport current equal to 300 A has been used with a residual resitivity ratio of copper equal to 100.

Fraction of current into HTS lead matrix (%)	**Temperature at connection (K)**
1	35.5
2	37.5
3	39.4
4	41.3
5	43.1
6	44.9
Sensitivity [K/A]	0.63

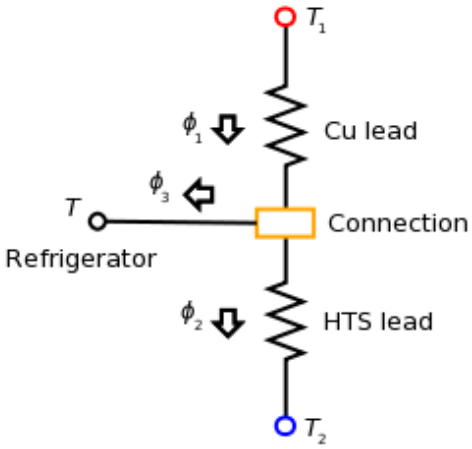

Figure D.1: Schematic drawing of a full current lead on which the analytical model is based.

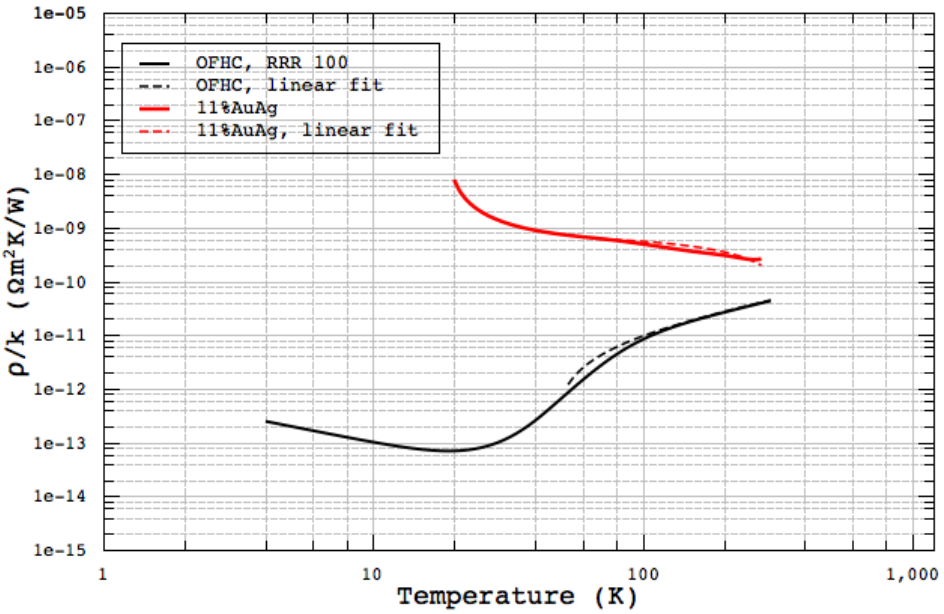

Figure D.2: Ratio of electrical resitivity to thermal conductivity of OFHC copper (RRR 100) and 11%AuAg.

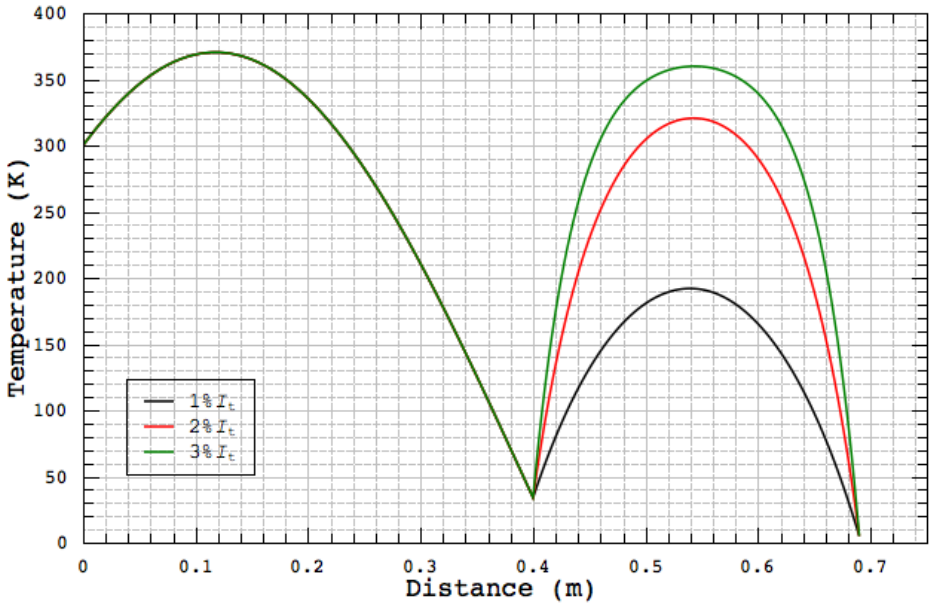

Figure D.3: Results of analytical analysis of full current leads. A transport current equal to 300 A is flowing through the lead. It is assumed that a certain percentage of transport current, I_t, is flowing through the matrix of the HTS lead in steady state.

Appendix E

Cast3M: layout of the code

Cast3M is a software which is graciously available for research and academic use. It is based on an object-oriented language, Gibiane, developped at the Commissariat à l'Energie Atomique (CEA) located in France. Because of its historical developement, it is not an end user application as ANSYS [18] may appear. Hence, additional functions and a modified solver have been added to the original library to study the thermal behavior of MICE spectrometer. Figure E.1 (page 63) shows the map of the code specific to the study of MICE cryogenic system. Figure E.2 (page 64) gives the procedures developped for this particular task. [1].

The code have been commented using Doxygen syntax [20].

[1] Maps created with XMind [19].

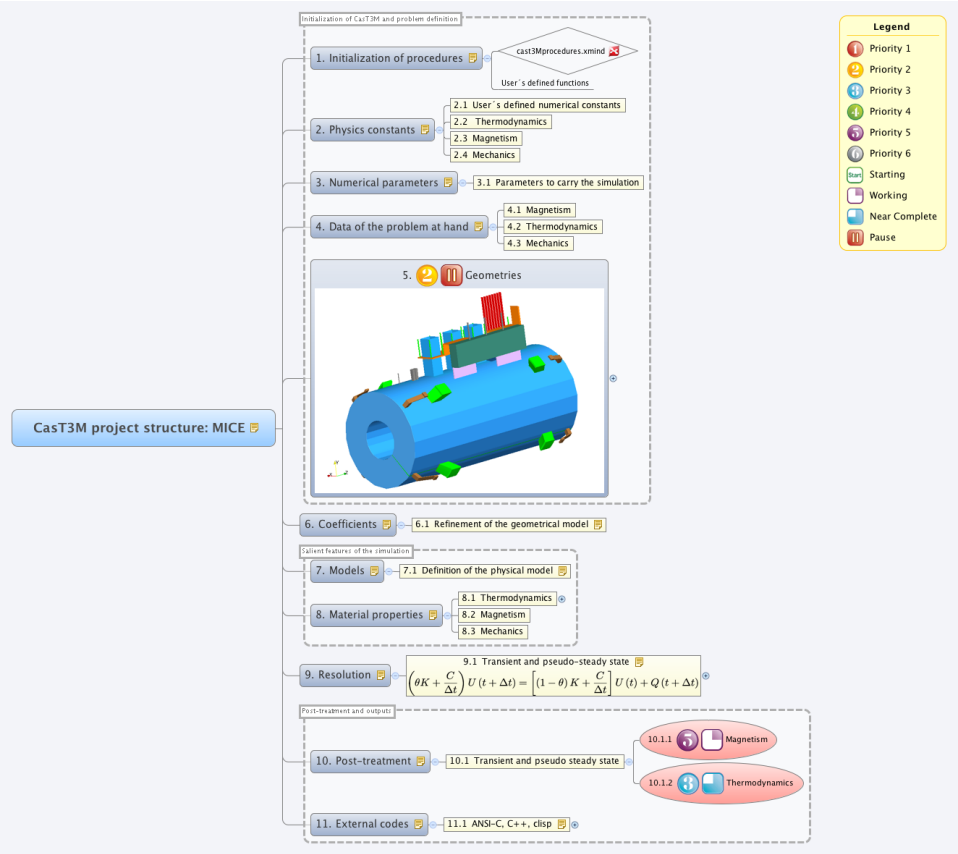

Figure E.1: Map of the program to study MICE cryogenic system.

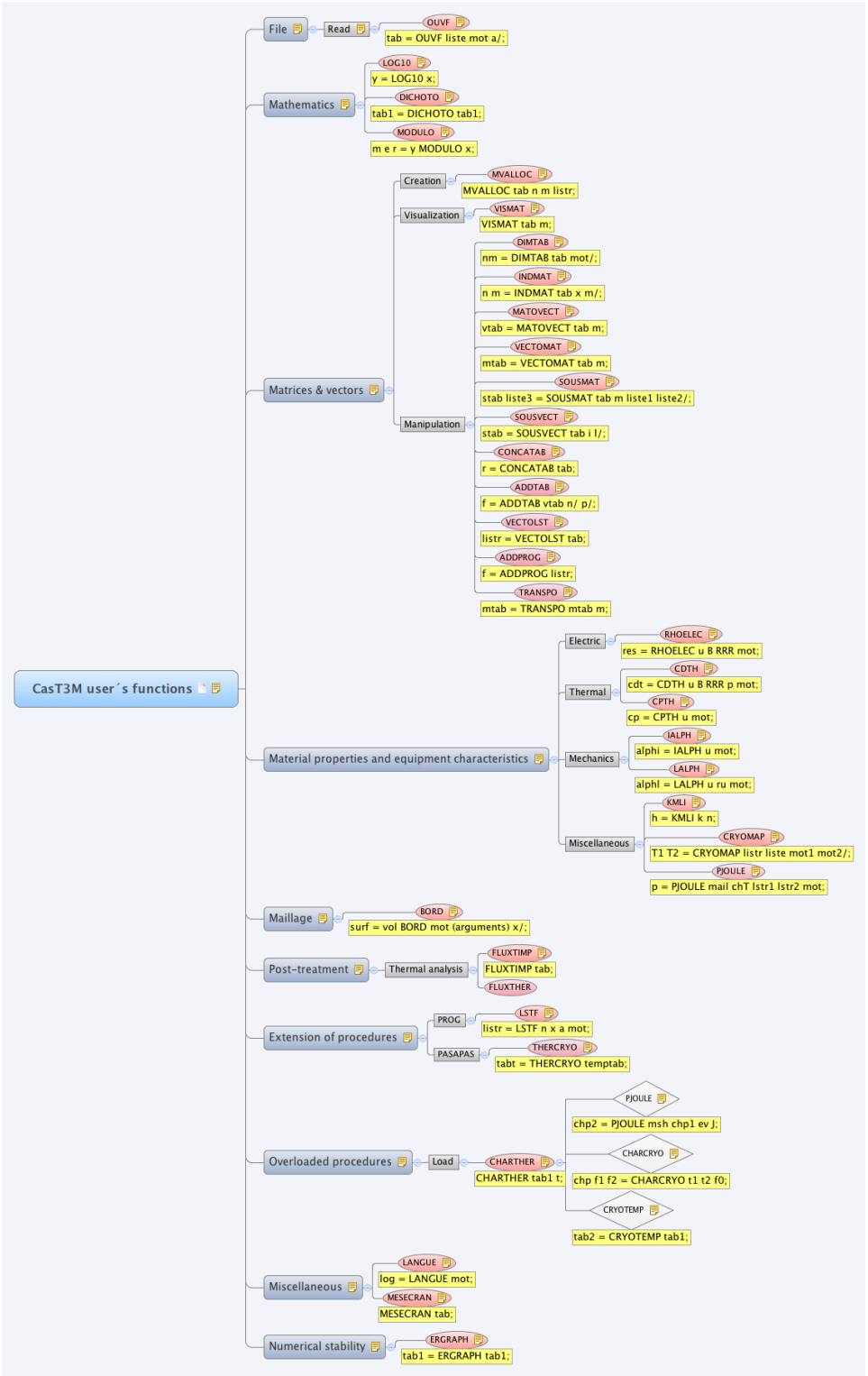

Figure E.2: Map of the procedures developped in the framework of MICE project

Appendix F

Listing of codes

F.1 Preamble

This appendix gathers some of the codes used to performed computation. It does not include the gibiane files. Indeed, it is composed of a larger number of lines which would represent a total of more than 200 pages of listing. However, it is available upon contacting the author at the following email address:

frederic.trillaud.work@gmail.com.

The headers are not included in the listings because of legal issues. Some of the fits used in the description of the material properties were extracted from Cryocomp® software [21].

F.2 C and C++ codes

F.2.1 50K bracket of the 25T cold mass support

```
////////////
/// C++ ///
////////////

/*
 *  FILE: g10straptemperature.cpp
 *
 *  AUTHOR: Frederic Trillaud
 *  LABORATORY: LBL
 *  DATE: 7/30/09
 *
 *  INTRODUCTION: Estimation of the temperature at the 50K brackets (L006) of
 *  the 25T cold mass supports (L000).
 */


///////////////
/// HEADERS ///
///////////////

#include <iostream>
#include "../Headers/thermalconductivity.h"
```

```
#include "../Headers/integration.h"


//////////////////
/// CONSTANTS ///
//////////////////

#define nn 294


///////////////
/// ROUTINE ///
///////////////

using namespace std;

int main()
{
double x0;

system("clear");

cout << "****************" << endl;
cout << "G10 straps, MICE" << endl;
cout << "****************" << endl;
cout << " Initial value, x0: " << endl;
cin >> x0;

double x=x0+10, y=0, z=0;
double l1=0.1668, l2=0.3668 , l3=0.508;
double A1=0.0006, A2=0.0006, A3=0.0002;
double T_1=300, T_2=4.2, T_3=84;
double R_1, R_2, R_3;
double a11, a12, a13, a22, a23, a33;
double b1=T_1, b2=T_1-T_2, b3;
double RRR_Cu=100, B=0;
double epsi=1e-2;
double k_G10[nn], k_Cu[nn];
int T[nn];
double k_G10av1, k_G10av2, k_Cuav3;
int i;
int T0 = 4;

for (i = 0; i < nn; i++)
{
T[i]=T0+i;
k_G10[i]=conductivity(T, B, RRR_Cu, 0, 1, 0, "G10");
k_Cu[i]=conductivity(T, B, RRR_Cu, 0, 1, 0, "copper");
}

while (fabs(x0-x) > epsi)
{
k_G10av1=integration(T, k_G10, x0, T_1, "trapezoidal");
k_G10av1=fabs(k_G10av1);
k_Cuav3=integration(T, k_Cu, T_3, x0, "trapezoidal");
k_Cuav3=fabs(k_Cuav3);
k_G10av2=integration(T, k_G10, T_2, x0, "trapezoidal");
k_G10av2=fabs(k_G10av2);
R_1=(1/k_G10av1)*(l1/A1);
R_2=(1/k_G10av2)*(l2/A2);
R_3=(1/k_Cuav1)*(l3/A3);
a11=1;
```

```
a12=R_1/R_2;
a13=R_1/(R_2*(R_3+R_1)+R_3*R_1);
a22=1/R_1;
a23=R_3/(R_2*(R_2*(R_3+R_1)+R_3*R_1));
a33=1/(R_2*(R_3+R_1)+R_3*R_1);
b1=T_1;
b2=T_2-T_3;
b3=R_2*(T_3-T_1)+R_1*(T_3-T_2);
z=a33*b3;
y=a22*b2+a23*b3;
x=x0;
x0=a11*b1+a12*b2+a13*b3;
}

cout << "**************************" << endl;
cout << "Temperature (K): " << x0 << endl;
cout << "Heat flux, phi1 (W): " << y+z << endl;
cout << "Heat flux, phi2 (W): " << y << endl;
cout << "Heat flux, phi3 (W): " << z << endl;
cout << "**************************" << endl;
cout << "Frederic Trillaud, LBNL 2009" << endl << endl;

return 0;
}
```

F.2.2 Copper and HTS current leads

```
/////////
/// C ///
/////////

/*
 *  FILE: cuhtsleads.c
 *
 *  AUTHOR: Frederic Trillaud
 *  LABORATORY: LBL
 *  DATE: 7/30/09
 *
 *  INTRODUCTION: Computation of the temperature profile across the copper
 *  and HTS current leads.
 */


///////////////
/// HEADERS ///
///////////////

#include <stdio.h>
#include <math.h>


/////////////////
/// CONSTANTS ///
/////////////////

#define nn 1000
#define pi 3.14159265


///////////////
/// ROUTINE ///
///////////////
```

```
int main(){

FILE *f1;
f1 = fopen("cuhtscurrentleads.dat", "w");

double UT[nn];
double UZ[nn];

double pp = 0.06;
double It = 300;
double UU;
double l1 = 0.4, l2 = l1+0.29;
double A1 = pi*pow(0.00265, 2), A2 = 8e-7;
double a1 = 1.757e-13, a2 = 2e-12, b1 = 6.57e-13, b2 = 6.5e-10;
double Tr1 = 50, Tr2 = Tr1;
double T1 = 300, T2 = 5;
double k1 = 400, k2 = 45;
double p0 = -59.5, p1 = 2.236;
double J1 = It/A1, J2 = pp*It/(0.6*A2);
double omega1 = sqrt(a1)*J1, omega2 = sqrt(a2)*J2;
double F1 = -b1*pow(J1, 2), F2 = -b2*pow(J2, 2);
double beta = (k1*A1*omega1)/(k2*A2*omega2);
double a = T1-Tr1-(F1/pow(omega1, 2));
double e1 = (Tr1+F1/pow(omega1, 2))-(Tr2-F2/pow(omega2, 2))+a*cos(omega1*l1);
double e2 = beta*a*sin(omega1*l1)-(1/(k2*A2*omega2))*(p0+p1*(Tr2-F2/pow(omega2, 2)));
double e3 = T2-Tr2+F2/pow(omega2, 2);
double gamma1 = beta+(p1/(k2*A2*omega2)-1)*tan(omega1*l1);
double gamma2 = beta+(p1/(k2*A2*omega2)+1)*tan(omega1*l1);
double g1 = ((beta*e1+(tan(omega1*l1))*e2)/gamma1)-e3*exp(-omega2*(l2-l1));
double g2 = gamma2/gamma1-exp(-2*omega2*(l2-l1));
double d = g1/g2;
double c = (beta*e1+(tan(omega1*l1))*e2)/gamma1-d*gamma2/gamma1;
double b = (c+d-e1)/sin(omega1*l1);

int i;
for (i = 0; i < nn; i++){
UZ[i] = i*(l2/(nn-1));
        if (UZ[i] <= l1)
        UU = Tr1+F1/pow(omega1, 2)+a*cos(omega1*UZ[i])+b*sin(omega1*UZ[i]);
        else
        UU = Tr2-F2/pow(omega2, 2)+c*exp(omega2*(UZ[i]-l1))+d*exp(-omega2*(UZ[i]-l1));
UT[i] = UU;
if ((UZ[i] <= (l1+0.001)) && (UZ[i] >= (l1-0.001)))
printf("%g %g\n", UZ[i], UT[i]);
}

int ii;
for (ii = 0; ii < nn; ii++)
fprintf(f1, "%g %g \n", UZ[ii], UT[ii]);

fclose(f1);

return 0;
}
```

Appendix G

Example of convergence

Figure G.1 (page 70) shows one of the convergence result. It was obtained for a typical case at full transport current without the presence of nitrogen tank.

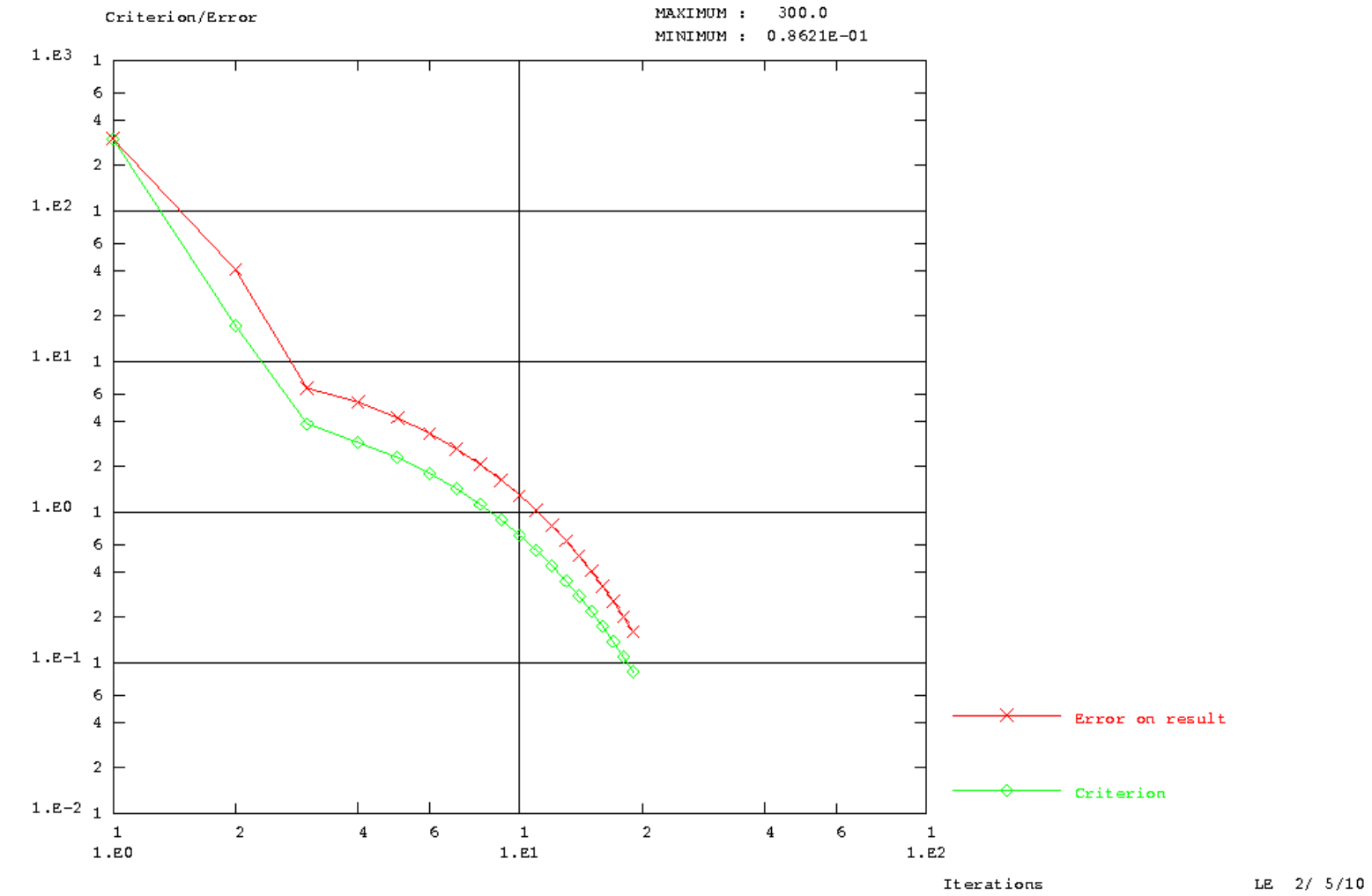

Convergence on criterion and error on result, lumped cryo-refrigerators

Figure G.1: Example of convergence for a typical case at full transport current without the presence of the nitrogen tank.

Bibliography

[1] Cryomech, Inc. Cryo-refirgeration. http://www.cryomech.com/.

[2] Jack W. Ekin. *Experimental Techniques for Low-Temperature Measurements*. OXFORD University Press, 2006.

[3] Alain Blondel. International Muon Ionization Cooling Experiment. http://www.mice.iit.edu/.

[4] WangNMR, Inc. Custom designs of superconducting magnets. http://www.wangnmr.com/main.htm.

[5] Commissariat à l'Energie Atomique CEA - DEN/DM2S/SEMT. Cast3M 2009. http://www-cast3m.cea.fr/cast3m/index.jsp.

[6] Kitware, Inc. and Los Alamos National Laboratories. Paraview 3.8. http://www.paraview.org/.

[7] Thomas William and Colin Kelley. Gnuplot 4.4.0. http://www.gnuplot.info/index.html.

[8] Ion Vasilief. QtiPlot 0.9.7.9. http://soft.proindependent.com/qtiplot.html.

[9] John W. Eaton. Octave 3.2.3. http://www.gnu.org/software/octave/.

[10] GNU Project. GNU Compiler Collection. http://gcc.gnu.org/.

[11] P. Fabbricatore. private communications, November 13, 2009.

[12] Paul Nicholson. A program to compute Air Core Mutual Inductances. http://abelian.org/acmi/.

[13] Erik Krooshoop. A program to compute solenoid inductances. h.j.g.krooshoop@utwente.nl.

[14] Y. Iwasa. *Case Studies in Superconducting Magnets, Design and Operational Issues*. Springer, 2$^{\cdot nd}$ edition, 2009.

[15] WangNMR, Inc. Final engineering design for mice spectrometer solenoid magnets. Technical report, WangNMR, Inc., 2006. LBL P.O. 6806258.

[16] Y. Iwasa. *Case Studies in Superconducting Magnets, Design and Operational Issues*. Plenum Press, New York, 1994.

[17] HTS-110 Inc. Technical data. http://www.hts110.co.nz/our-products/current-leads/.

[18] ANSYS, Inc. ANSYS 12. http://www.ansys.com/.

[19] XMind Ltd. XMind 3.1. http://www.xmind.net.

[20] Dimitri Van Heesch. Doxygen 1.6.3. http://www.stack.nl/ dimitri/doxygen.

[21] Eckels Engineering, Inc. CRYOCOMP™. http://www.cryodata.com/. not maintained, see METALPAK, EXPAK and CPPAK.